hydrology

MDPI

Article

Impacts of Climate Change and Variability on Precipitation and Maximum Flows in Devil's Creek, Tacna, Peru

Edwin Pino-Vargas [1], Eduardo Chávarri-Velarde [2,*], Eusebio Ingol-Blanco [2,*], Fabricio Mejía [1], Ana Cruz [1] and Alissa Vera [1]

[1] Department of Civil Engineering, Universidad Nacional Jorge Basadre Grohmann, Tacna 23000, Peru; epinov@unjbg.edu.pe (E.P.-V.); 20210308@lamolina.edu.pe (F.M.); acruzb@unjbg.edu.pe (A.C.); averam@unjbg.edu.pe (A.V.)
[2] Department of Water Resources, Universidad Nacional Agraria La Molina, Lima 15024, Peru
* Correspondence: echavarri@lamolina.edu.pe (E.C.-V.); eingol@lamolina.edu.pe (E.I.-B.)

Abstract: Global projections of climate change indicate negative impacts on hydrological systems, with significant changes in precipitation and temperature in many parts of the world. As a result, floods and droughts are expected. This article discusses the potential effects of climate change and variability on the maximum precipitation, temperature, and hydrological regime in Devil's Creek, Tacna, Peru. The outputs of precipitation and daily temperature of fifteen regional climate models were used for the RCP4.5 and RCP8.5 emission scenarios. The methodology used includes the bias correction and downscaling of meteorological variables using the quintiles mapping technique, hydrological modeling, the evaluation of two emission scenarios, and its effect on the maximum flows of the stream. The results of the multi-model ensemble show that the maximum annual precipitation will probably increase by more than 30% for the RCP4.5 and RCP8.5 scenarios for the 2021–2050 period relative to the 1981–2005 period. Likewise, as expected, the maximum flows could increase by 220% and 154% for the RCP4.5 scenarios for the 2021–2050 and 2051–2080 terms, respectively, and 234% and 484% for the RCP8.5 scenarios and for the 2021–2050 and 2051–2080 terms, respectively, concerning the recorded historical value, increasing the probability of flood events and damage in populations located downstream.

Keywords: maximum precipitation; maximum flow; climate change; hydrological modeling

Citation: Pino-Vargas, E.; Chávarri-Velarde, E.; Ingol-Blanco, E.; Mejía, F.; Cruz, A.; Vera, A. Impacts of Climate Change and Variability on Precipitation and Maximum Flows in Devil's Creek, Tacna, Peru. *Hydrology* **2022**, *9*, 10. https://doi.org/10.3390/hydrology9010010

Academic Editors: Carmelina Costanzo, Tommaso Caloiero and Roberta Padulano

Received: 23 November 2021
Accepted: 30 December 2021
Published: 5 January 2022

1. Introduction

Changes in temperature and precipitation patterns, due to the increase in greenhouse gas concentrations, affect hydrological processes. Consequently, negative impacts are expected on water resources for agriculture, urban uses, mining, industry, aquatic life in rivers and lakes, and hydroelectric power production. Similarly, spatial changes in the intensity and frequency of precipitation can affect the magnitude and frequency of flows, increasing the intensity of floods and droughts, with important impacts on economic activities at the local and regional levels [1,2].

On the other hand, on a global scale, studies show that the temperature increases by more than 3.5 °C, under the RCP8.5 emission scenario. By the end of the 21st century, precipitation is projected to reduce by more than 20% for medium and low latitudes [3]. Similarly, an increase in evaporation and a decrease in soil moisture content and groundwater recharge are expected. Consequently, drought conditions and increased evapotranspiration rates are projected for summer in subtropical regions, as well as medium and low latitudes [3].

In Peru, a national evaluation of climate scenarios carried out by the Peruvian National Meteorological and Hydrological Service (SENAMHI), estimated a progressive increase in the maximum and minimum temperature, by 2.8 °C on average by the end of the 21st century. Similarly, a reduction in precipitation of 40% is projected for winter, and an average increase of 20% during summer and spring [4].

An increase in temperature with a decrease in precipitation will produce a drastic decrease in water availability in rivers and other natural sources, as well as a substantial increase in evapotranspiration rates, meaning greater water consumption, affecting agricultural and municipal uses, and the production of electrical and industrial energy. Additionally, a slow but sustained reduction in glaciers in Peru is expected, which plays an important role in the supply of water to the water systems of communities in the Andean regions.

On the other hand, many regions of the north, center, and south of Peru are frequently seriously affected by floods and huaycos (debris flow and mudslides) as a result of high-intensity precipitation which occurs in the basins, influenced by the El Niño phenomenon. It is estimated that 26 El Niño events have occurred during the 20th century. The most severe events occurred in 1924–1925, 1982–1983, 1997–1998 [5], and most recently in 2016–2017. These events have generated great damages and economic losses in the social, productive, and infrastructure sectors. The total sectoral damages caused by the El Niño phenomena 1982–1983 and 1997–1998 were around USD 3200 million and USD 3500 million, respectively, including direct and indirect damages [6]. In the latest 2016–2017 event, total damages were estimated to be around USD 4 billion [7].

Similarly, at the JORGE BASADRE rain gauge, located in the city of Tacna, precipitation of 5.1 mm was recorded in 24 h in 2017, constituting one of the highest values ever recorded for November. The intensities were variable and covered a large part of the coastal zone of the Tacna region [8].

On the other hand, extreme precipitation events are commonly represented using IDF precipitation curves. Extreme weather events are becoming more severe and frequent, which leads to uncertainties as to how prepared the infrastructure is to face these changes. Infrastructure designs are based on the IDF precipitation curves with the assumption of stationarity, which means that the statistical properties of future events will be similar to those of the past [9,10]. However, climate change is expected to alter climate extremes, a concept called non-stationarity [11].

The main objective of this research is to evaluate the potential impacts of climate change and variability on precipitation and maximum flows in the Devil's Creek, located in the Tacna region, Peru. The Tacna region is located in the northern region of the Atacama Desert. The Atacama Desert is one of the largest hyper-arid deserts in the world [12].

For this purpose, the outputs of the meteorological variables of fifteen regional climate models of the Coupled Model Intercomparison Project Phase 5 [13] were used as inputs for the hydrological model. A bias correction was applied for temperature and precipitation using the quantile mapping method [14–17], which enables bias correction of the regional climate model simulations in comparison with the data observed in rain gauges. The changes in precipitation and maximum flow were evaluated for the period 2021–2050 and the RCP4.5 (intermediate) and RCP8.5 (high) emission scenarios.

The results, in combination with the evaluation of the maximum precipitation and temperature, the analysis of frequencies, and hydrological modeling, will help to answer the research questions such as: What would be the changes of the maximum precipitation and temperature in the sub-basin of the Devil's Creek under historical conditions and climate change scenarios? What changes would the frequency of maximum flows experience in the study area under scenarios of variability and climate change? What are the differences between historical conditions and climate change?

2. Materials and Methods

2.1. Precipitation Data and Historical Temperature

Historical data of daily precipitation and temperature of five (5) rain gauges near the study basin (Figure 1) were collected and analyzed for the period 1966–2020. The completion and extension of information were carried out with the Climatol software, which uses an approach based on the method used by Paulhus and Kohler [16] to complete the missing daily precipitation data. This consists of spatial interpolation of the normal

precipitation rate of neighboring rain gauges. This proportion method is extended in the Climatol package with options to use differences and full standardization to normalize the data [18]. However, because the JORGE BASADRE rain gauge only had daily precipitation data since 1993 (Table 1), and because a minimum period of 30 years is necessary, for analysis of the frequency of maximum precipitation, it was considered appropriate to evaluate information from the product named PISCO (Peruvian Interpolated data of the SENAMHI Climatological and hydrological Observations. Precipitation v2.0) [19], available from SENAMHI (National Service of Meteorology and Hydrology of Peru). To use these data, they had to be corrected using the quantile mapping technique and validated for the Devil's Creek area using local rain gauges (JORGE BASADRE, Calana, Calientes, Sama Grande, and Palca) as reference rainfall or observed values. These data have made it possible to complete the daily precipitation dataset for the JORGE BASADRE rain gauge, from 1981–1992.

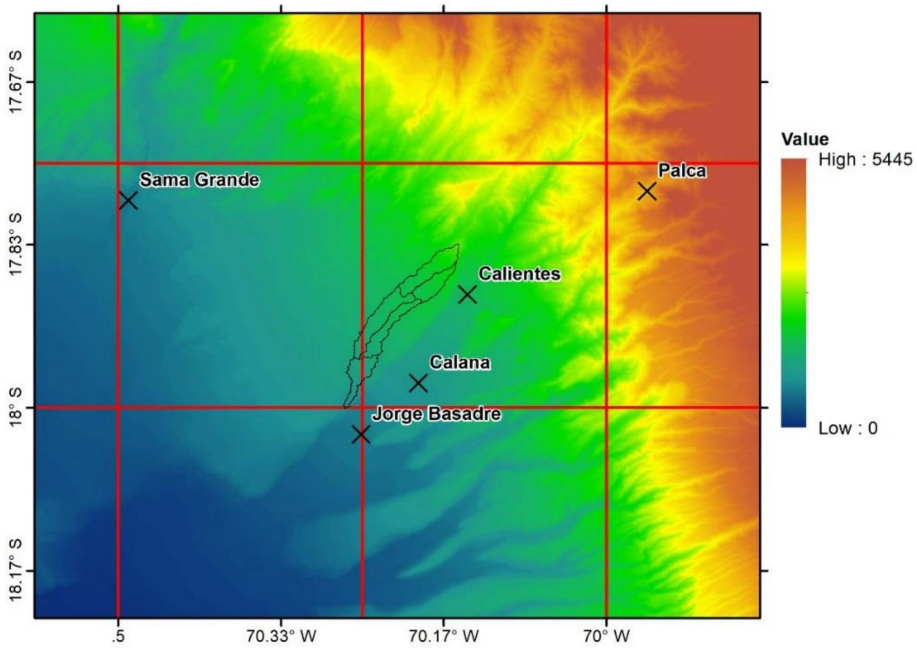

Figure 1. Location of the Devil's Creek with the meteorological rain gauges selected for the downscaling and cells of the general circulation models (GCMs).

Table 1. Availability of precipitation data.

Rain Gauge	No. Values	Start Date	Final Date	% Gaps	Duration (Years)
Calana	19,704	1 January 1966	31 December 2020	2	55
JORGE BASADRE	9952	1 January 1993	31 December 2020	3	28
Calientes	19,298	1 January 1966	31 December 2020	4	55
Sama Grande	19,789	1 January 1966	31December 2020	1	55
Palca	15,866	1 July 1966	31 December 2020	20	55

2.2. General Circulation Models and Scenarios

When considering climate change, one of the challenges water resource managers often face is deciding which general circulation models (GCMs) should be used to assess the impacts of climate change on water resource systems. This is a puzzling question because all GCMs demonstrate uncertainty in the prediction of historical climate variables [20,21]. However, some criteria, such as spatial resolution, the degree of atmospheric–ocean coupling, and the availability of multiple realizations, can be taken into account when selecting

a set of GCMs to reduce uncertainties in the predictions of maximum precipitation and floods based on any individual GCM [2,22,23]. Considering the high degree of uncertainty that climate models present in the projection of precipitation, fifteen regional climate models have been deemed convenient to be evaluated in this research.

Currently, there are regionally scaled models (25 km × 25 km) whose outputs still need bias correction and spatial downscaling to improve their performance in a particular region. This research uses 15 general circulation models of the CMIP5 project (the NASA NEX-GDDP dataset–Coupled Model Intercomparison Project Phase 5): ACCESS1-0, bcc-csm1-1, CanESM2, CCSM4, CESM1-BGC, CNRM-CM5, CSIRO-Mk3-6-0, GFDL -CM3, GFDL-ESM2G, GFDL-ESM2M, IPSL-CM5A-LR, MIROC-ESM, MIROC-ESM-CHEM, MIROC5, MPI-ESM-LR, MPI-ESM-MR [24].

On the other hand, climate data from the downscaled emission scenarios RCP4.5 (intermediate emission) and RCP8.5 (high emissions) are used. These scenarios have been selected based on their emission trajectories; medium and high, respectively, for the period 2021–2080.

2.3. Bias Correction and Downscaling

Downscaling can be defined as a technique that increases the resolution of GCMs to obtain the climate at a local scale. There are two fundamental methods for downscaling large-scale data from GCM results: statistical and dynamic downscaling. Their concepts have been discussed in various articles [25–28]. This research uses a statistical downscaling of the outputs of the previously described regional models. Quantile mapping is applied to perform bias correction in regional climate model simulations compared to observed data. This method is designed to fit the distribution of the modeled data, so that they match observed climate data [29,30]; in this case, precipitation and temperature. The following expression was applied and resolved in Rstudio to find the corrected future value:

$$y^{f}_{corr,i} = F_y^{-1}\left(F_x\left(x^{f}_{i}\right)\right) \quad (1)$$

where $y^{f}_{corr,i}$ is the future value corrected at time i, and F_x (x), F_y (y) represent the empirical cumulative distribution functions of the model (x) and observations (y). To perform bias correction and the downscaling, this study uses a historical period and a base period simulated by climate models, both from January 1981 to December 2005. With this, the correction for the future period 2021–2080 is applied.

2.4. Climate Model Ensembles

The evaluation of the capacity of a climate model to simulate trends in extreme events is complex due to internal climate variability, whose simulated phases are unique for the realization of each model [31]. On the other hand, we know that, currently, the models have improved a lot in projecting the future climate. However, a high degree of uncertainty still persists, showing great variability between models in mainly projecting precipitation. In this sense, the multi-model ensembles highlight the uncertainty in climate predictions that result from structural differences in global climate models, as well as the uncertainty due to variations in the initial conditions or parameterizations of the model [32]. Similarly, several investigations have shown that a weighted ensemble method, based on the simulation performance of the models, may have better projection abilities than the equal-weighted ensembles [33–36].

In this study, the ensemble of downscaled climate scenarios of the 14 global circulation models (GCMs) applied to the Devil's Creek is given by the weighted average whose weights are determined according to the performance of each model concerning the historical period 1981–2005. The determination of the weights of each GCM is determined by the genetic algorithm [37], whose objective function is to minimize:

$$F_{obj} = min \sum_{j=1981}^{2005} \left(P_{hist,j} - \sum_{i=1}^{14} \left(w_i * P_{GCM,j} \right) \right)^2 \quad (2)$$

where P_{hist} is the historical maximum annual precipitation for the Devil's Creek, for the year j, P_{GCM} is the maximum annual precipitation of the GCM of the Devil's Creek, and w is the weight of each GCM. The objective is to minimize the error between the observed value and the simulated value, optimizing the weights that each model would have based on its performance with the history.

The proposed objective function is interpreted as the ensemble of the 14 GCMs in the Devil's Creek for the period 1981–2005 to be identical to the maximum annual precipitation generated in the creek.

The genetic algorithm begins with an initial population subjected to the selection process of the objective function evaluation to later apply the genetic crossing and mutation operators. These are responsible for diversifying the individuals of the initial population [37,38]. A simple ensemble with equal weighting is used for the minimum and maximum temperatures.

2.5. Hydrological Modeling

2.5.1. Frequency Analysis of Total Daily Precipitation for the Northern Area of the City of Tacna

In the Caplina river basin, there are five rain gauges: two main climate rain gauges (La Yarada and Calana), two ordinary rain gauges (Calientes and Palca), and a main agricultural climate rain gauge (JORGE BASADRE) [39]. Due to its proximity to the city of Tacna, the total daily precipitation recorded at the JORGE BASADRE rain gauge was considered representative of the northern area of the city of Tacna. This rain gauge has a continuous record of 28 years (1993 to 2020) (Figure 2). The frequency analysis was performed from the partial duration series, which was adjusted to the Gumbel distribution.

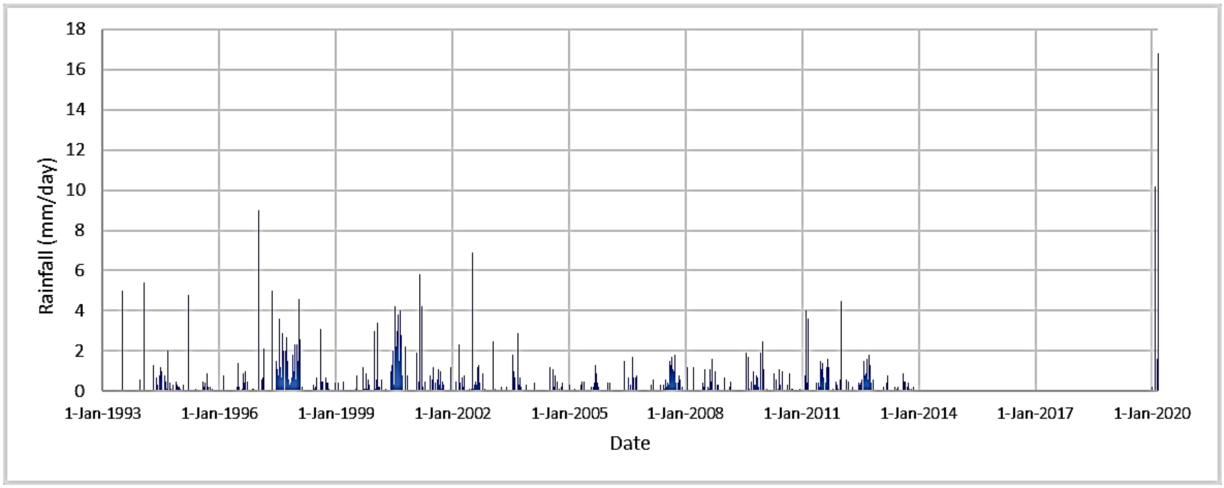

Figure 2. Total daily precipitation—JORGE BASADRE rain gauge.

Figure 3 shows that the precipitation event recorded on 21 February 2020 has a return period of 255.8 years.

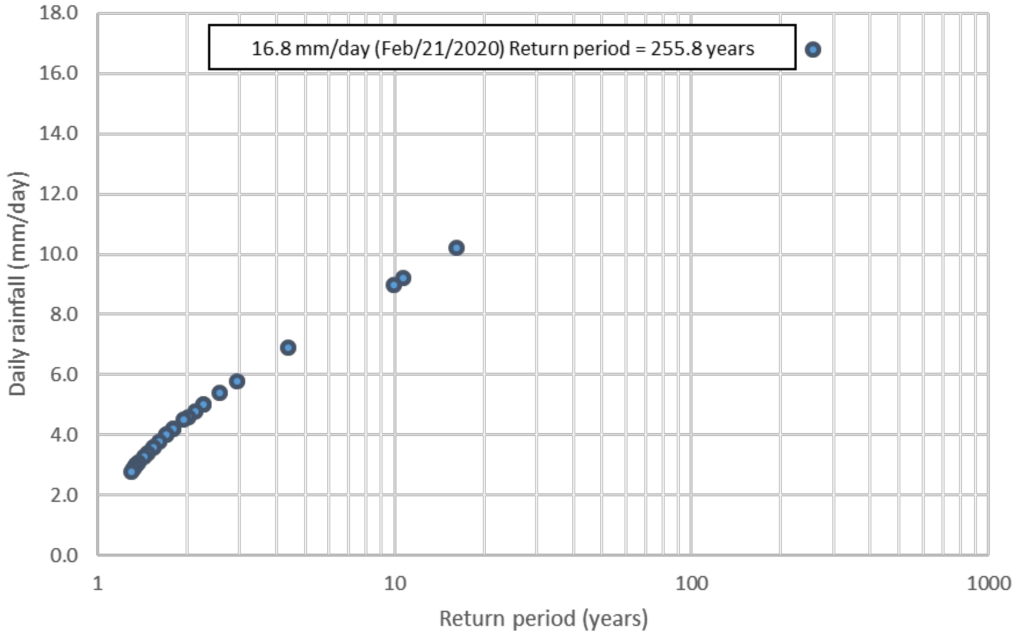

Figure 3. Frequency analysis of the partial series of total daily precipitation at JORGE BASADRE rain gauge (from 1993 to 2020).

2.5.2. Estimated Precipitation Events for the Devil's Creek

Figure 4 shows the comparison of the total daily rainfall discharged from the PISCO product for the coordinates of the JORGE BASADRE rain gauge and the total daily rainfall from the JORGE BASADRE rain gauge, during the period 1 January 1993 to 21 April 2014.

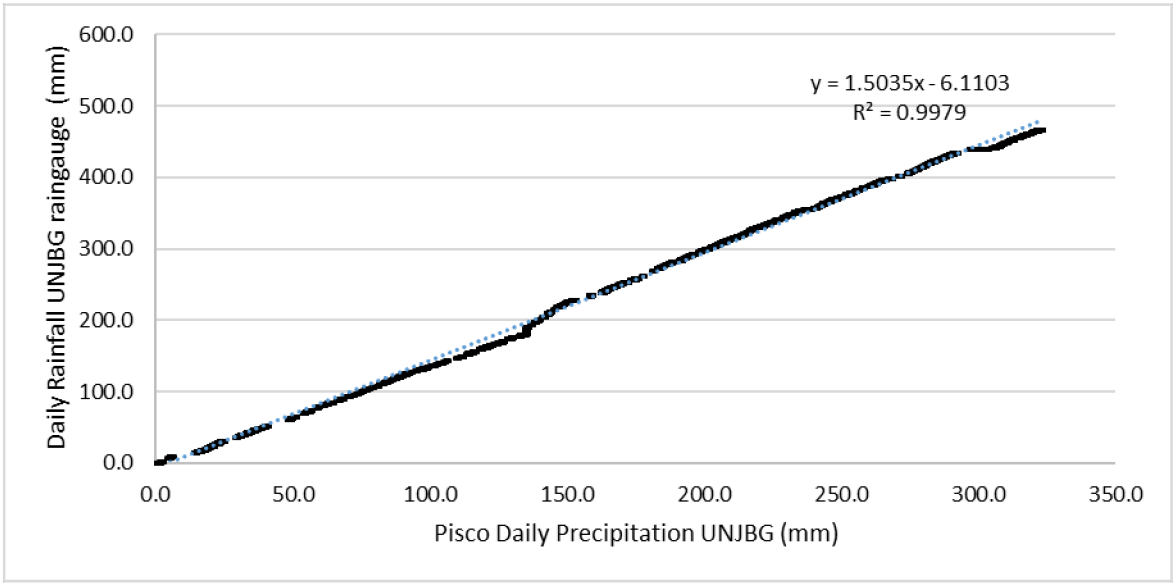

Figure 4. Comparison double-mass between the precipitation data of the PISCO product in JORGE BASADRE rain gauge and the rainfall of the JORGE BASADRE rain gauge, during 7780 days (1 January 1993–21 April 2014).

The efficiency criterion used to evaluate the similarity of the daily rainfall at the JORGE BASADRE rain gauge and the PISCO daily precipitation was the Nash–Sutcliffe model. The efficiency criterion of Nash and Sutcliffe efficiency (E) is defined by the following equation [40].

$$E = 1 - \frac{\sum_1^N (O_i - P_i)^2}{\sum_1^N (O_i - \overline{O})^2} \quad (3)$$

where O_i is the daily rainfall recorded, P_i is the PISCO daily precipitation, $\overline{O}$ is the mean daily rainfall recorded, and N is the number of observations. The ranges of E lay between 0.75 and 1.0 (Very good), 0.65 and 0.75 (Good), 0.5 and 0.65 (Satisfactory), and $\leq$0.5 (Unsatisfactory).

The Nash–Sutcliffe efficiency index of the PISCO product was 0.83, which shows a very good correspondence between the series indicated above [41]. Likewise, it was found that the difference between the total daily precipitation depth discharged from the PISCO product for the coordinates of the JORGE BASADRE rain gauge with respect to the total daily rainfall (depth) from the JORGE BASADRE rain gauge was −31%. Similarly, it was found that the difference between the total daily precipitation depth discharged from the PISCO product for the coordinates of the middle and upper parts of the Devil's Creek with respect to the total daily precipitation depth discharged from the PISCO product for the JORGE BASADRE rain gauge was −6%. Figure 5 shows a comparison of the total daily rainfall discharged from the PISCO product for the coordinates of the middle and upper parts of the Devil's Creek and the total daily rainfall from the JORGE BASADRE rain gauge discharged from the PISCO product, during the period 01 January 1993 to 21 April 2014.

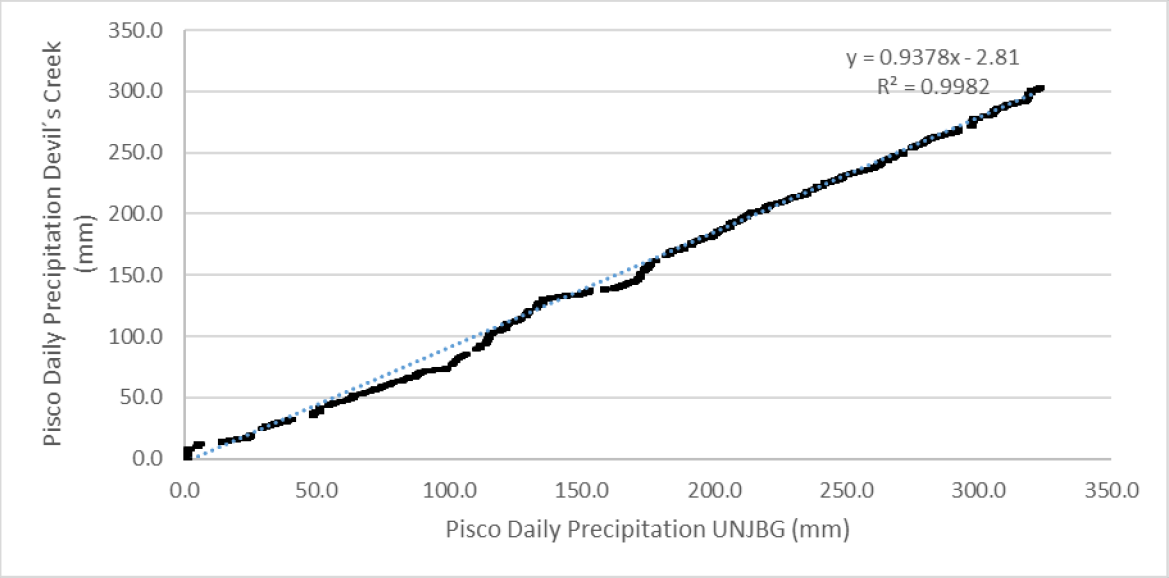

Figure 5. Comparation double-mass between the precipitation data of the PISCO product in the JORGE BASADRE rain gauge versus the precipitation data of the PISCO product in Devil's Creek over 7780 days (1 January 1993–21 April 2014).

On the other hand, the FIAG UNJBG automatic rain gauge has continuously recorded precipitation every 30 min from 7 December 2019 to the present (7 May 2021). Given that the FIAG UNJBG automatic rain gauge is located near the JORGE BASADRE rain gauge, it was assumed that the precipitation which falls every 30 min in the middle and upper parts of the Devil's Creek differed by −38% with respect to FIAG UNJBG automatic rain gauge. The calculations are as follows:

- JORGE BASAGRE rain gauge = 1.31 × PISCO precipitation in JORGE BASADRE;
- PISCO precipitation for the coordinates of the middle and upper parts of the Devil's Creek × 1.06 = PISCO precipitation in JORGE BASADRE;
- The FIAG UNJBG automatic rain gauge is located near the JORGE BASADRE rain gauge; therefore, we assumed that the rainfall data of the FIAG UNJBG automatic rain gauge were the same that the rainfall data of the JORGE BASADRE rain gauge;
- Then, PISCO precipitation for the coordinates of the middle and upper parts of the Devil's Creek × 1.38 = Rainfall data of the FIAG UNJBG automatic rain gauge. The value 1.38 is a result of 1.31 × 1.06.

Considering this, the estimated precipitation for the middle and upper parts of the Devil's Creek for the period 7 December 2019 to 7 May 2021 is shown in Figure 6. In that period, three main events have been identified.

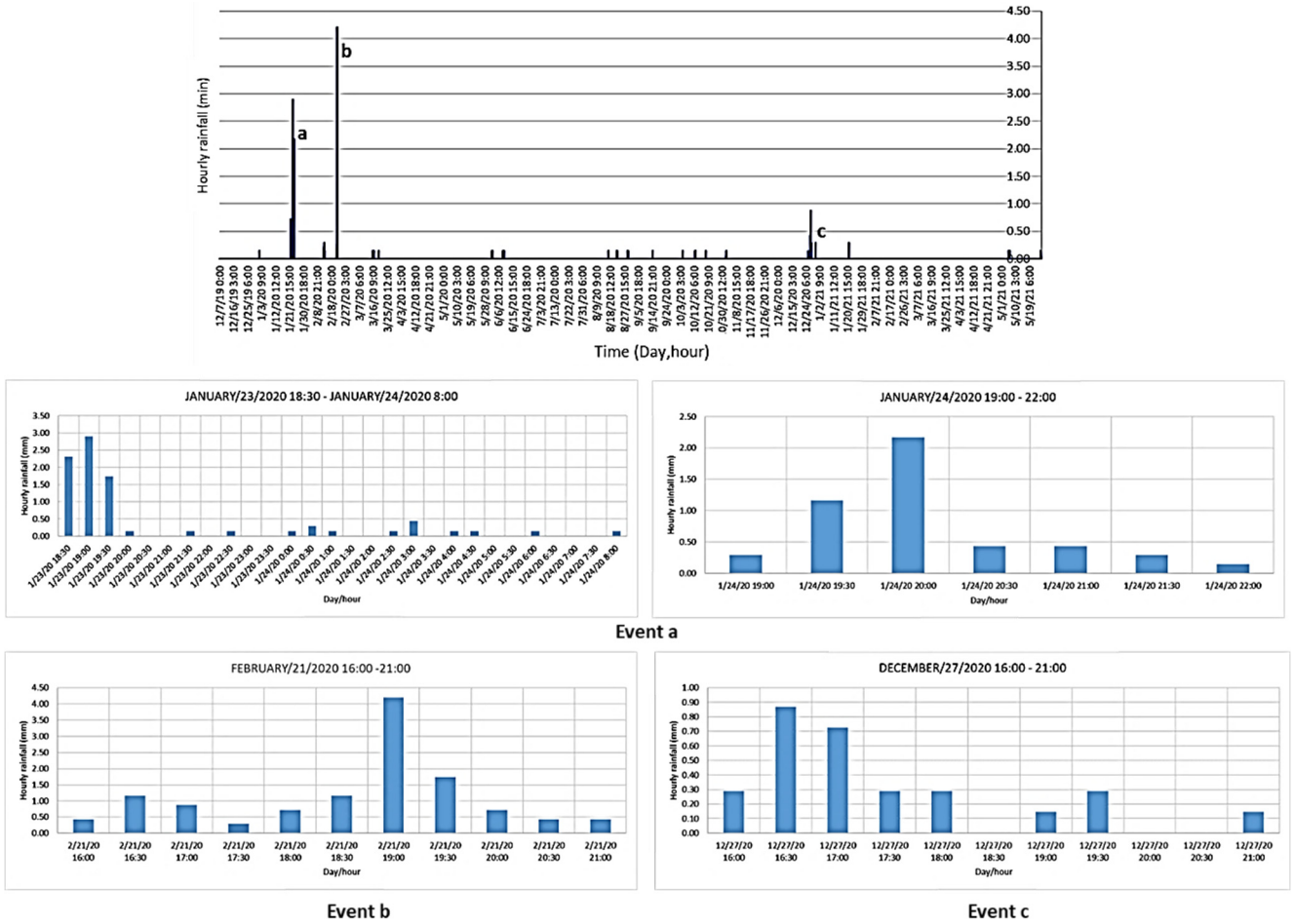

Figure 6. Estimated hourly rainfall for the Devil's Creek. (**a**) Event on 23–24 January 2020; (**b**) event on 21 February 2020; and (**c**) event on 27 December 2020.

In order to corroborate the lower amount of precipitation in the Devil's Creek concerning the FIAG UNJBG automatic rain gauge, a space–time analysis of the information recorded at the JORGE BASADRE rain gauge was carried out with other daily satellite products, such as IMERG and CHIRPS. To do this, two virtual rain gauges were defined to be compared with the JORGE BASADRE rain gauge. Table 2 shows the location of each of the aforementioned rain gauges.

Table 2. Virtual rain gauges and JORGE BASADRE rain gauge.

No	Rain Gauge	Length	Latitude	Elevation (masl)	Source	Record
1	Jorge Basadre G.	−70.2515°	−18.0268°	552	UNJBG	1993–2014, 2017–2021
2	EV01	−70.25°	−17.95°	941	-	-
5	EV02	−70.15°	−17.85°	1560	-	-

Additionally, Figure 7 shows the location of the aforementioned rain gauges. The two virtual rain gauges are located in the lower and upper parts of the basin. It should be noted that the quadrants correspond to the available satellite information.

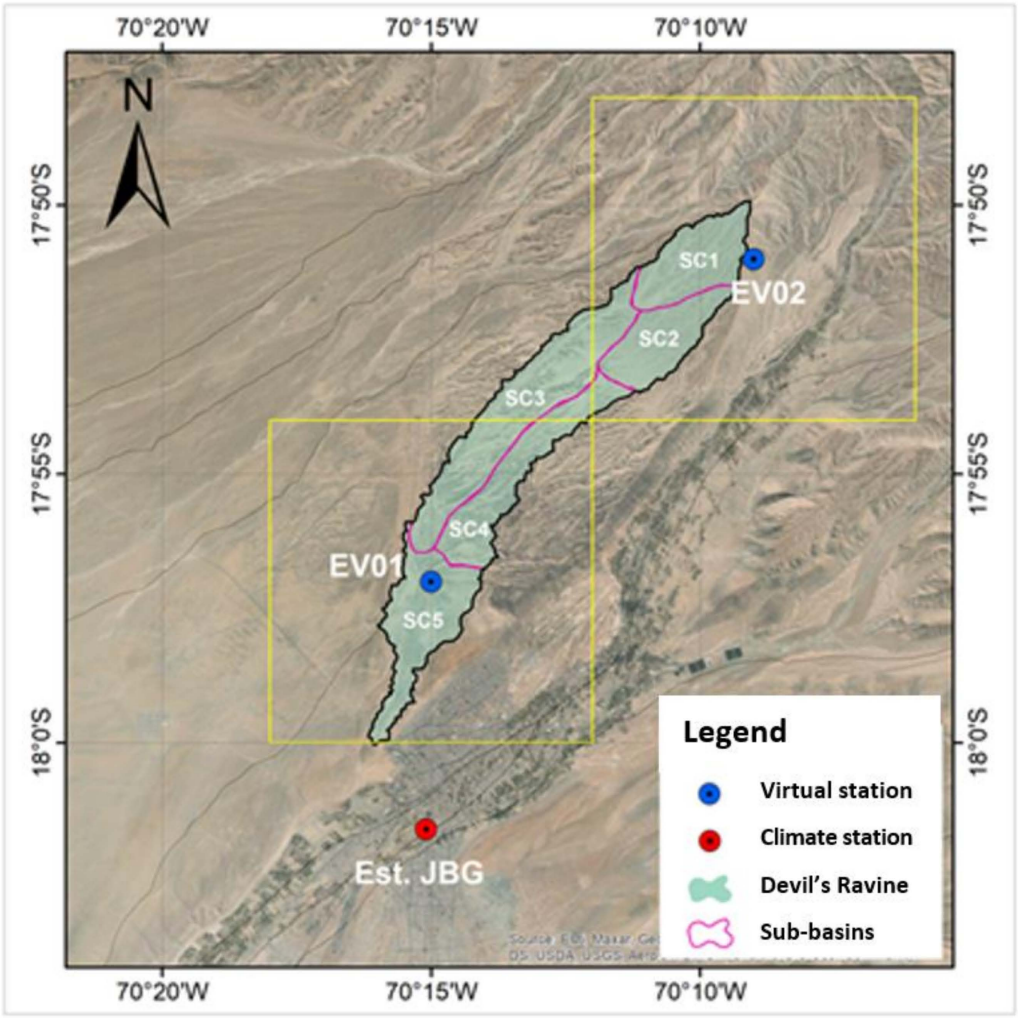

Figure 7. Location of virtual rain gauges and the JORGE BASADRE rain gauge.

For the spatial analysis of precipitation, three satellite products were used, as shown in Table 3. Similarly, for the IMERG product, the early and final versions were used. The information for each product was the total daily precipitation.

In the case of the IMERG product, the information was available from 2000 to date, and in the case of CHIRPS, the information was complete for the entire analysis period.

Figure 8 shows the series of total daily precipitation data from the JORGE BASADRE rain gauge and the series of each satellite product downloaded for the same coordinate from the JORGE BASADRE rain gauge. It can be seen that the data downloaded for the total daily precipitation of the IMERG Early product slightly overestimated the precipitation, and the IMERG Final product underestimated the precipitation information at the JORGE

BASADRE rain gauge. In contrast, the data downloaded for the total daily precipitation of the CHIRPS product were greater than the data for the total daily precipitation of the JORGE BASADRE rain gauge.

Table 3. Satellite and data base products analyzed.

Product	Version	Abbreviation	Source	Resolution	Frequency	Term
Peruvian Interpolated data of SENAMHI's Climatological and Hydrological Observations	V. 2.1	PISCO	SENAMHI	0.1° × 0.1°	Daily	1981–2016
Integrated Multi-satellite Retrievals for GPM	Early V06B	IMERG-F	NASA	0.1° × 0.1°	Daily and 30 min	2000–2021
Integrated Multi-satellite Retrievals for GPM	Final V06B	IMERG-E	NASA	0.1° × 0.1°	Daily and 30 min	2000–2021
Climate Hazards group Infrared Precipitation with Rain gauges	V. 2.0	CHIRPS	UCSB (ˣ)	0.05° × 0.05°	Daily	1981–2021

(ˣ) University of California Santa Bárbara.

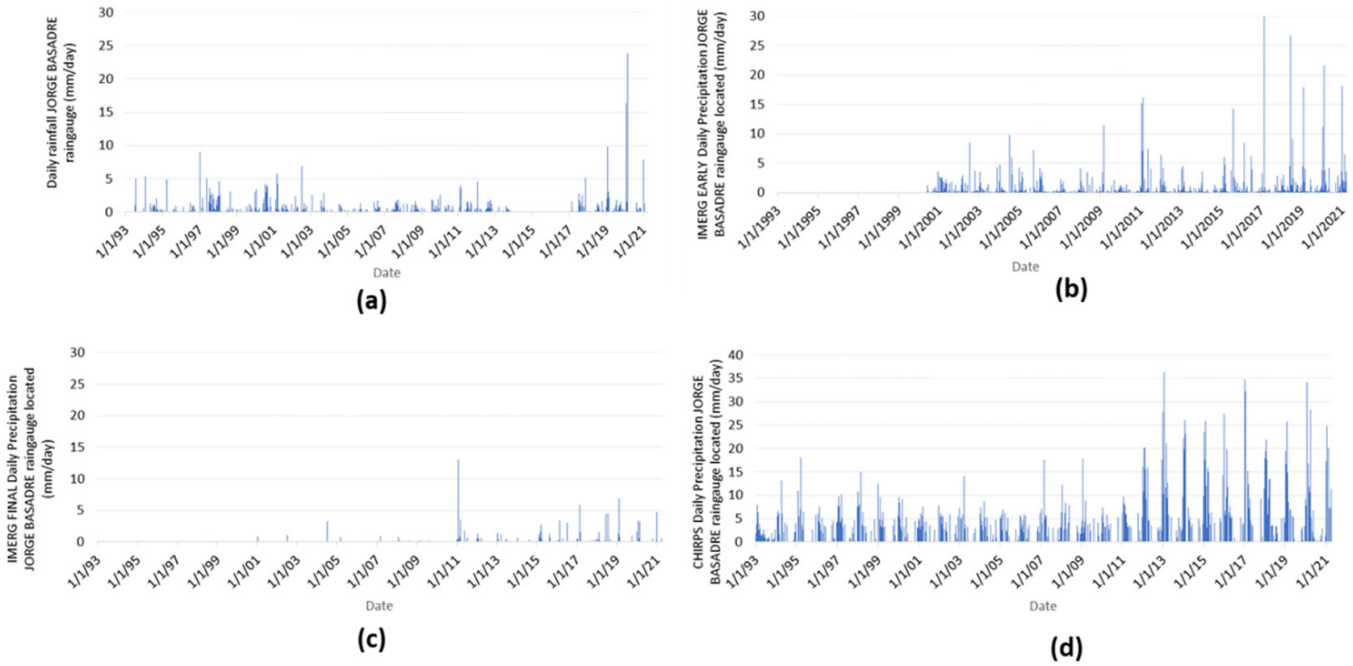

Figure 8. Comparation between (**a**) daily rainfall in JORGE BASADRE rain gauge and daily precipitation from satellites products: (**b**) IMERG Early, (**c**) IMERG Final, and (**d**) CHIRPS.

Although the information from the satellite products used does not have a good correlation with the data observed from the JORGE BASADRE rain gauge, a spatial correlation between them can be determined to establish indicators of spatial variation. The spatial correlation was carried out between the three established rain gauges: JORGE BASADRE rain gauge, Virtual Rain Gauge 01 (lower part of the Creek), and Virtual Rain Gauge 2 (upper part of the creek).

Figure 9 shows the results of the correlations made concerning the JORGE BASADRE rain gauge and the virtual rain gauges EV01 and EV02. With the IMERG Early product, the results obtained were that the precipitation in the EV01 area was 40% lower than the precipitation in the JORGE BASADRE rain gauge, whereas the EV02 rain gauge area had 41% less precipitation than the JORGE BASADRE rain gauge area. Similarly, with the IMERG Final product, the results obtained were that the precipitation in the EV01 area was

33% lower than the precipitation in the JORGE BASADRE rain gauge, whereas the EV02 rain gauge area had 71% less precipitation than the zone of JORGE BASADRE rain gauge.

Concerning the CHIRPS product, the precipitation in the EV01 and EV02 zones was lower by 27% and 45%, respectively, in comparison to the JORGE BASADRE rain gauge. In summary, the previous results corroborate that the amount of precipitation in the Devil's Creek was less than the amount of precipitation in the city of Tacna, during the period of common observation between them.

Table 4 shows a summary table of the linear regression coefficients obtained in the comparison of the data series. It is observed that the area of the EV01 virtual rain gauge, on average, would have 31% less precipitation than the JORGE BASADRE rain gauge, whereas the area of the EV02 virtual rain gauge would have 51.7% less precipitation than the JORGE BASADRE rain gauge.

Table 4. Summary of the regression coefficients and percentage between the JORGE BASADRE rain gauge and the virtual rain gauge (EV01 and EV02).

Virtual Rain Gauge	PISCO JB Rain Gauge	IMERG Early JB Rain Gauge	IMERG Final JB Rain Gauge	CHIRPS JB Rain Gauge	Mean	EV01 and EV02 Have Less Precipitation than JORGE BASADRE Rain Gauge (%)
EV01	0.76	0.60	0.67	0.73	0.69	100% − 69% = 31.0%
EV02	0.51	0.59	0.29	0.54	0.483	100% − 48.3% = 51.7%

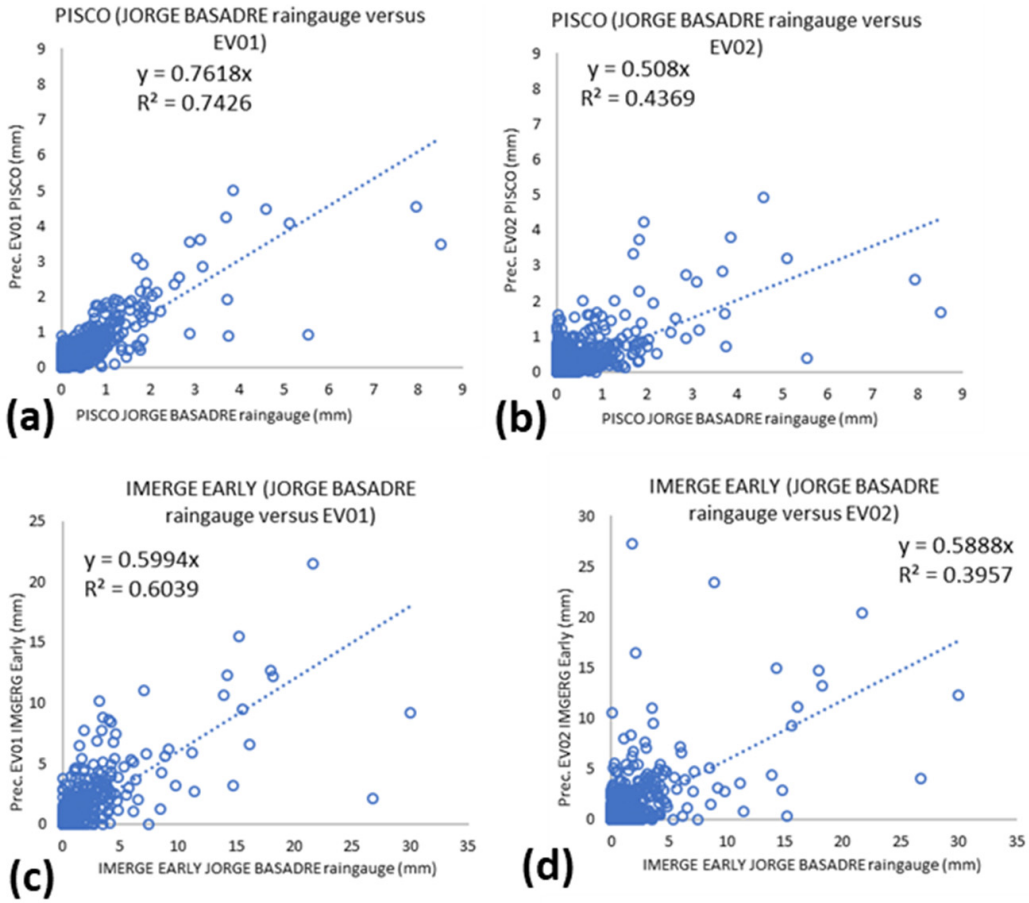

Figure 9. *Cont.*

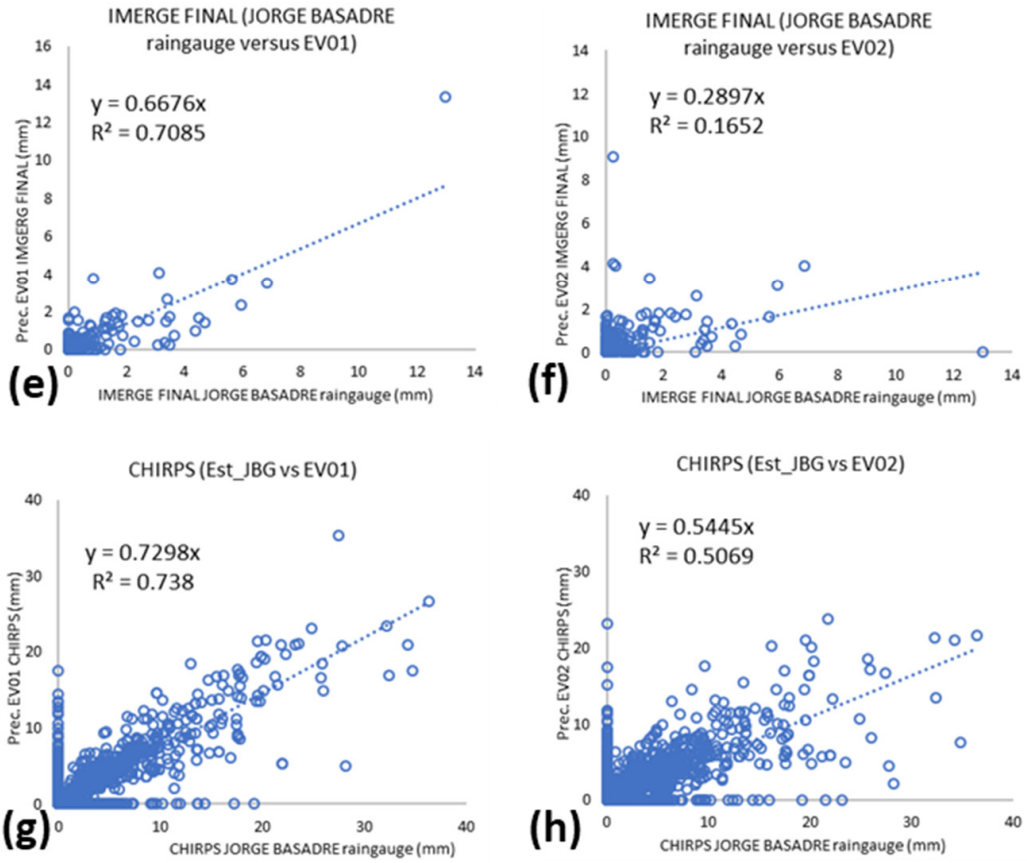

Figure 9. Correlations were made between the total daily precipitation data between the JORGE BASADRE rain gauge and the virtual rain gauges, (EV01 and EV02) using the products: (**a**,**b**) PISCO, (**c**,**d**) IMERGE Early, (**e**,**f**) IMERGE Final, and (**g**,**h**) CHIRPS.

2.5.3. Types of Soils and Infiltration Capacity in the Devil's Creek

Characterization of the soil type was carried out through field samplings conducted on 22 July 2020. Figure 10 shows the places where three soil samplings and the corresponding infiltration tests were carried out. The information on the infiltration tests is presented in Table 5.

Table 5. Location of sampling points, texture, infiltration equation, and hydraulic conductivity at saturation (Ks).

Sampling	UTM Coordinates	Texture	Infiltration Equation F (mm), t (min)	Ks (mm/min)
1	368477E, 8019016N	Clayey silt	$F = 4.0\ t^{0.81}$	0.872
2	368477E, 8019035N	Sandy silt with gravel and clay	$F = 3.67\ t^{0.87}$	1311
3	368328E, 8018959N	Sandy silt with gravels	$F = 7.2\ t^{0.72}$	0.749

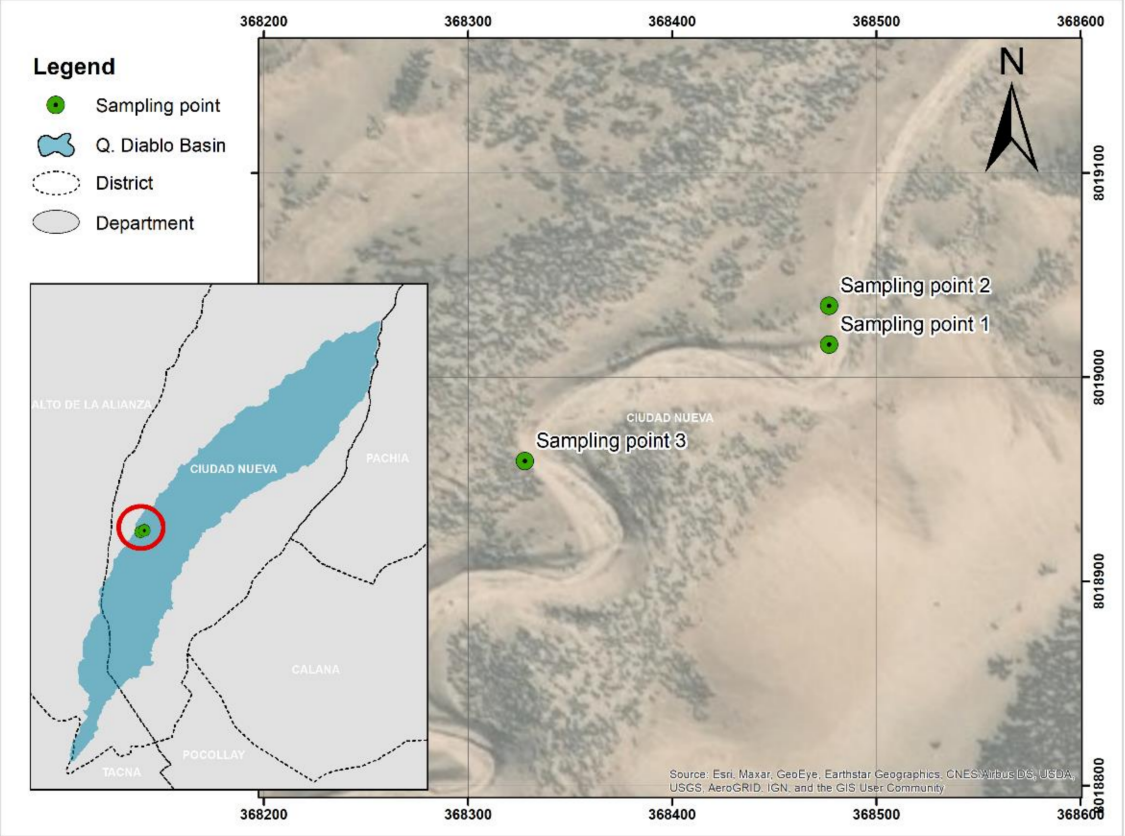

Figure 10. Location of soil sampling points.

2.5.4. Hydrological Model of the Devil's Creek

Hydrological modeling of the maximum flow produced in the Devil's Creek was carried out using the RS MINERVE program.

The RS MINERVE program is open access and widely used in Peru and national institutions such as the National Water Authority (ANA, by its abbreviation in Spanish) and the Potable Water and Sewerage Service of Lima (SENAMHI, by its abbreviation in Spanish) [42].

The RS MINERVE program is a flow simulation program which allows the modeling of complex hydraulic and hydrological networks following a semi-distributed approach. The program is capable of representing not only the main hydrological processes such as snow and glacier melting, surface and sub-surface runoff, but also regulatory infrastructure such as retention dams, spillways, water intakes, turbines, and pumps, among others.

RS MINERVE integrates different hydrological precipitation-runoff models such as GSM, SOCONT, SAC-SMA, GR4J, and HBV. Likewise, it allows the inclusion of hydraulic structures through different models (reservoirs, turbines, spillways, etc.) [43].

The model used for the hydrological modeling of the Devil's Creek was the SOCONT (Soil CONTribution model). The SOCONT and GR4J models are more sensitive in extreme event modeling than the HBV and SAC models [44]. As shown in Figure 11, the SOCONT model procedure consists of the Snow-SD model simulating the evolution of the glacial layer (melting and accumulation) as a function of temperature (T) and precipitation (P), and calculating the equivalent precipitation (Peq). In the case of Devil's Creek, and because it is not a glacial stream, the equivalent precipitation constituted the precipitation. This equivalent precipitation was used as input to the GR3 model that takes into account the potential evapotranspiration (ETP) and generates the net intensity of rainfall for the SWMM model.

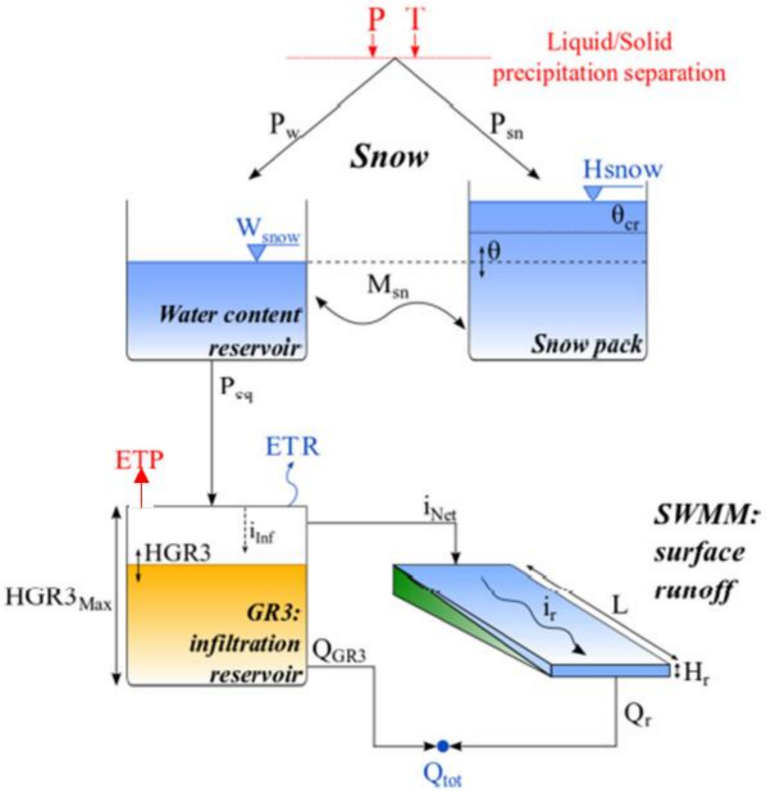

Figure 11. Composition of the SOCONT model.

The flow components of the SOCONT model are explained below:

- P: precipitation (L/T);
- T: Temperature (°C);
- P_w: Liquid precipitation (L/T);
- P_{sn}: Solid precipitation (L/T);
- P_{eq}: Equivalent precipitation (L/T) equal P_w (L/T), because there is no glacial area in the basin;
- i_{Inf}: Infiltration intensity (L/T)

  $i_{Inf} = P_{eq}\ (1 - (H_{GR3}/H_{GR3Max})^2)$, If $H_{GR3} \leq H_{GR3Max}$, where H_{GR3} (L) is the actual capacity of infiltration reservoir (L), and H_{GR3Max} (L) is the maximum capacity of the infiltration reservoir.

  $i_{Inf} = 0$, if $H_{GR3} > H_{GR3Max}$;
- ETR: Real evapotranspiration (L/T)

  $ETR = ETP\ \sqrt{H_{GR3}/H_{GR3Max}}$, If $H_{GR3} \leq H_{GR3Max}$

  $ETR = ETP$, If $H_{GR3} > H_{GR3Max}$;
- i_{Net}: Net intensity (L/T), $i_{Net} = P_{eq} - i_{Inf}$;
- Q_{GR3}: Base discharge (L^3/T)

  $Q_{GR3} = K_{GR3} \cdot H_{GR3} \cdot A$, If $H_{GR3} \leq H_{GR3Max}$, where K_{GR3} is the release coefficient of the infiltration reservoir (1/T) and A is the surface (L^2).

  $Q_{GR3} = K_{GR3} \cdot H_{GR3Max} \cdot A$, if $H_{GR3} > H_{GR3Max}$;
- I_r: Runoff intensity (L/T), $I_r = K_r \sqrt{J_0} H_r^{5/3} \cdot 1/L$, where K_r is the Strickler coefficient ($L^{1/3}/T$), J_0 is the average slope of the plane, H_r is the runoff water level downstream of the surface (L), and L is the length of the plane (L);
- Q_r: Surface runoff (L^3/T), $Q_r = I_r \cdot A$;
- Q_{tot}: Total runoff (L^3/T), $Q_{tot} = Q_{GR3} + Q_r$.

According to Table 6, the total number of parameters necessary for hydrological modeling is 16, of which 7 parameters are typical of the SOCONT model and also take into account 4 initial conditions.

Table 6. SOCONT model parameters and plugins [45].

Object	Name	Units	Description	Regular Range
SOCONT	A	m^2	Surface	>0
	S	mm/°C/d	Reference degree-day snowmelt coefficient	0.5 to 20
	SInt	mm/°C/d	Degree-day snowmelt coefficient	0 to 4
	Smin	mm/°C/d	Minimal degree-day snowmelt coefficient	≥0
	SPh	d	Phase shift of the sinusoidal function	1 to 365
	ThetaCri	-	Critical relative water content of the snow pack	0.1
	bp	d/mm	Melt coefficient due to liquid precipitation	0.0125
	Tcp1	°C	Minimum critical temperature for liquid precipitation	0
	Tcp2	°C	Maximum critical temperature for solid precipitation	4
	Tcf	°C	Critical snowmelt temperature	0
	HGR3Max	m	Maximum height of infiltration reservoir	0 to 2
	KGR3	1/s	Release coefficient of infiltration reservoir	0.00025 to 0.1
	L	m	Length of the plane	>0
	J0	-	Runoff slope	>0
	Kr	$m^{1/3}/s$	Strickler coefficient	0.1 to 90
	CFR	-	Refreezing coefficient	0 to 1
	SWEIni	m	Initial snow water equivalent height	-
	HGR3Ini	m	Initial level in infiltration reservoir	-
	HrIni	m	Initial runoff water level downstream of the surface	-
	ThetaIni	-	Initial relative water content in the snow pack	-

3. Results

3.1. Projected Maximum Annual Precipitation

3.1.1. Period 2021–2050

- RCP4.5 scenario

The maximum annual precipitation projected for the period 2021–2050 under the RCP4.5 emission scenario in the Devil's Creek is presented in Figure 12. The results show a variation range from 0.79 mm to 283 mm with an average of 5.64 mm and a standard deviation of 12.65 mm. The maximum value was projected by the model MPI_ESM_LR (the coupled Max Planck Institute Earth System Model). Likewise, the models bcc_csm1_1, CanESM2, CCSM4, GFDL_ESM2G, GFDL_ESM2M, MPI_ESM_LR projected maximum annual precipitation in a range of 27 mm to 283 mm. The bcc_csm1_1 and GFDL_ESM2M models predicted around 46 mm by 2034.

On the other hand, given the uncertainty in the projections, an arithmetic average of all models has been estimated, as well as an ensemble (dashed blue line) which has been calculated, assigning a greater weight to the model that has better performance concerning the maximum annual rainfall observed (see Equation (2)). The Access1-0 model was discarded from the analysis of maximum annual precipitation because it projected high values greater than 500 mm. The results of the assembly of the models indicate variation in the annual maximum daily precipitation from 2.77 mm to 24.70 mm, with an average of 5.70 mm for the period 2021–2050. The range of uncertainty in the predictions is shown in Figure 13, in which the linear extensions represent the highest and lowest values; the upper, central, and lower limits of the box represent the percentiles of 75%, 50%, and 25%, respectively; and the solid circles represent the outliers, which correspond to the maximum values predicted by each model.

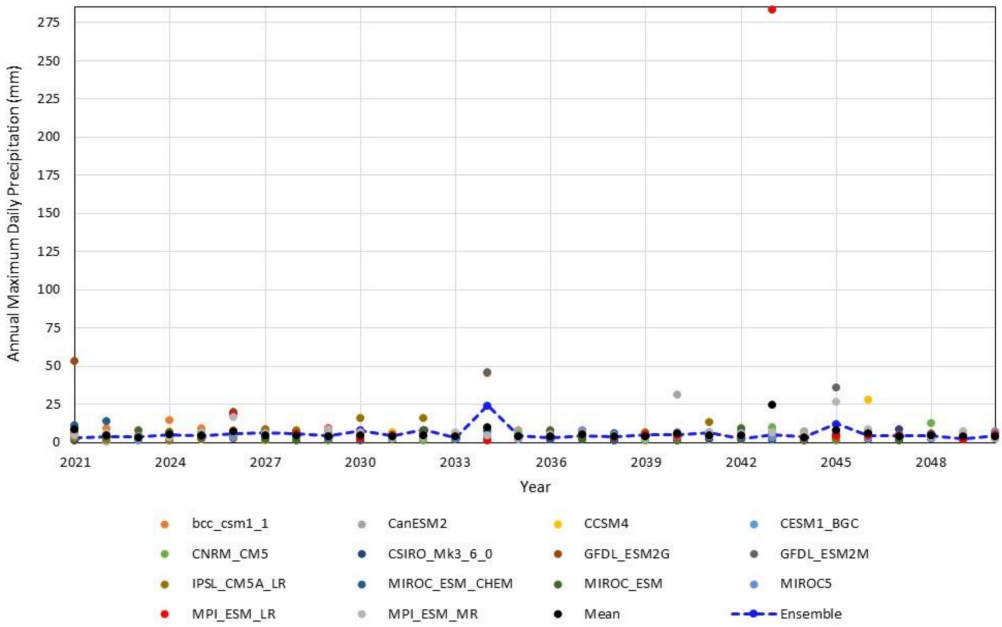

Figure 12. Annual maximum daily precipitation projected by 14 climate models under the RCP4.5 scenario for the Devil's Creek. The dashed blue line corresponds to the ensemble. Period: 2021–2050.

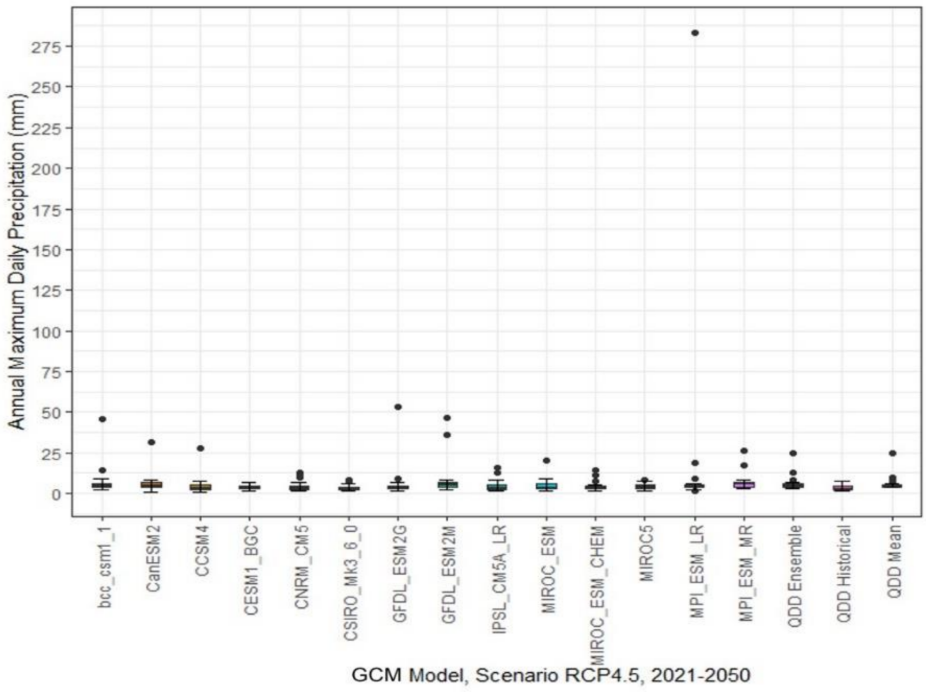

Figure 13. Boxplot for future projections of the annual maximum daily precipitation of 14 GCMs under the RCP4.5 scenario in the Devil's Creek, period 2021–2050. The linear extensions represent the highest and lowest values; the upper, middle and lower limits of the box represent the percentiles of 75%, 50%, and 25%, respectively; and the solid circles represent the outliers.

- RCP8.5 Scenario

The annual maximum daily precipitation projected for the 2021–2050 term under the RCP8.5 emission scenario in the Devil's Creek is shown in Figure 14. A varied range of 1.70 mm to 75.7 mm is evidenced with an average of 5.24 mm and a standard deviation of 3.29 mm for all models, indicating a low dispersion concerning the mean. The maximum

value was projected by the GFDL_ESM2M (Fluid Dynamics Laboratory (GFDL) GFDL-ESM2M model).

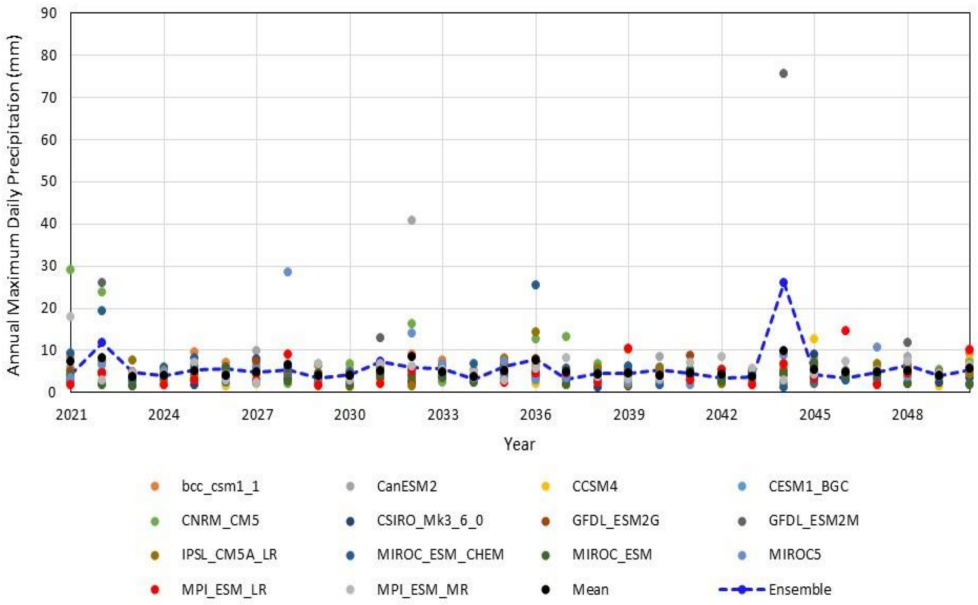

Figure 14. Annual maximum daily precipitation projected by 14 climate models under the RCP8.5 scenario for the Devil's Creek. The dashed blue line corresponds to the ensemble. Period: 2021–2050.

Likewise, the CanESM2, CNRM_CM5, GFDL_ESM2M, MIROC_ESM_CHEM, MIROC5 models projected the highest annual maximum precipitation values in a range of 25.5 mm to 75.7 mm, indicating that, in this period of analysis, heavy precipitation could occur in the Devil's Creek.

On the other hand, the results of the model ensemble indicate a variation in the maximum annual precipitation from 3.14 mm to 25.96 mm, with an average of 5.80 mm for the 2021–2050 term under the RCP8.5 scenario.

The range of uncertainty in the predictions is shown in Figure 15. Similarly, the linear extensions represent the highest and lowest values; the upper, central, and lower limits of the box represent the percentiles of 75%, 50%, and 25%, respectively; and the solid circles represent the outliers, which correspond to the maximum values predicted by each model.

3.1.2. Period 2051–2080

- RCP4.5 Scenario

The maximum annual precipitation projected for the period 2051–2080 under the RCP4.5 emission scenario in the Devil's Creek is shown in Figure 16. The results indicate a variation range from 0.86 mm to 95.46 mm with an average of 5.55 mm and a standard deviation of 5.20 mm for all models, indicating a low dispersion concerning the mean. The maximum value was projected by the CCSM4 model (The Community Climate System Model Version 4). Likewise, of the 14 models evaluated, 7 of them CCSM4, CNRM_CM5, GFDL_ESM2M, IPSL_CM5A_LR, MIROC_ESM_CHEM, MIROC5, MPI_ESM_LR projected the highest annual maximum precipitation values in a range of 21 mm to 96 mm, indicating that heavy precipitation could occur in the Devil's Creek during the analysis period under this emission scenario.

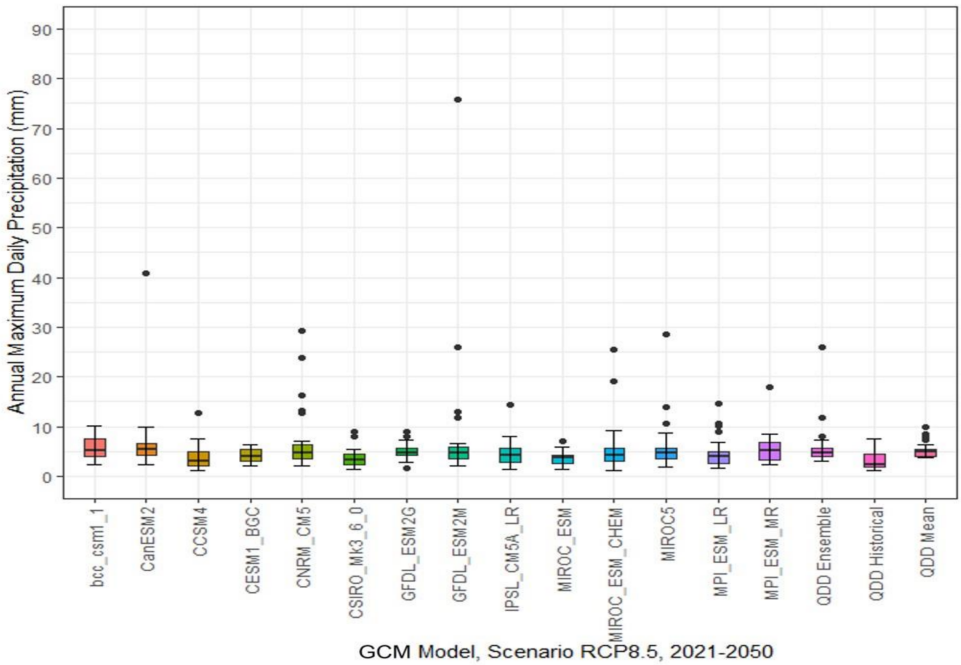

Figure 15. Boxplot for future projections of the annual maximum daily precipitation of 14 GCMs under the RCP8.5 scenario in the Devil's Creek, period 2021–2050. The linear extensions represent the highest and lowest values; the upper, middle and lower limits of the box represent the percentiles of 75%, 50%, and 25%, respectively; and the solid circles represent the outliers.

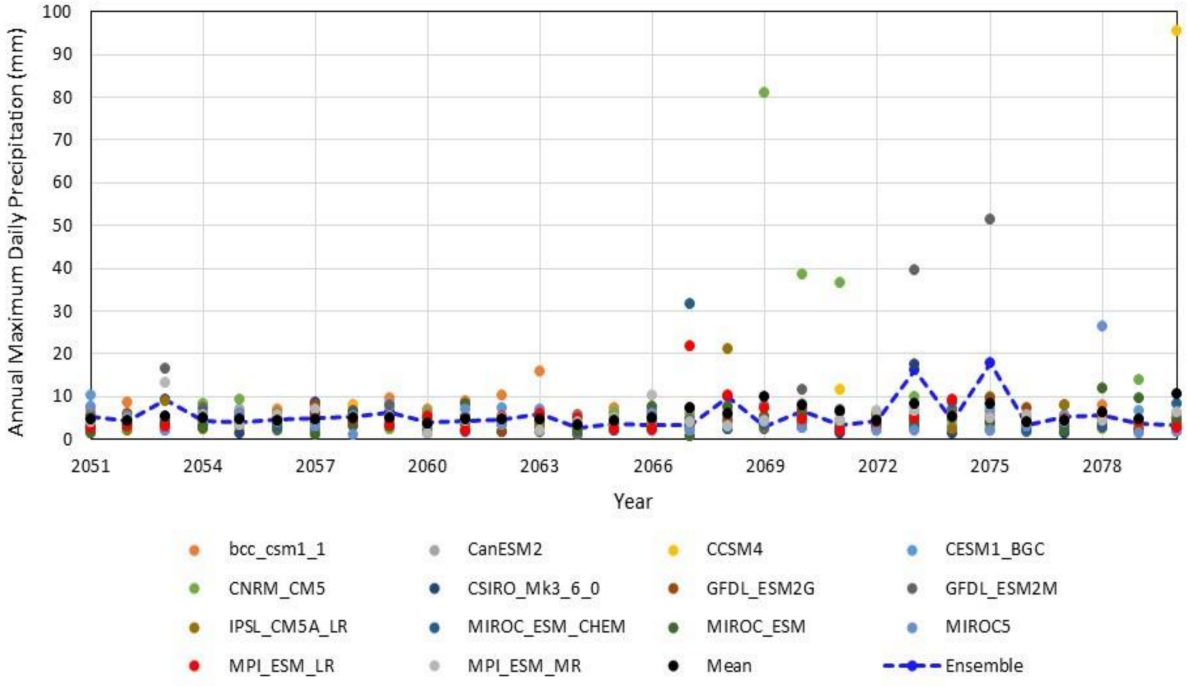

Figure 16. Annual maximum daily precipitation projected by 14 climate models under the RCP4.5 scenario for Devil's Creek. The dashed blue line corresponds to the ensemble. Period: 2051–2080.

On the other hand, the results of the model ensemble indicate a variation in the maximum annual precipitation from 2.77 mm to 17.86 mm, with an average of 5.60 mm for the 2051–2080 term under the RCP4.5 scenario. The range of uncertainty in the predictions is presented in Figure 17.

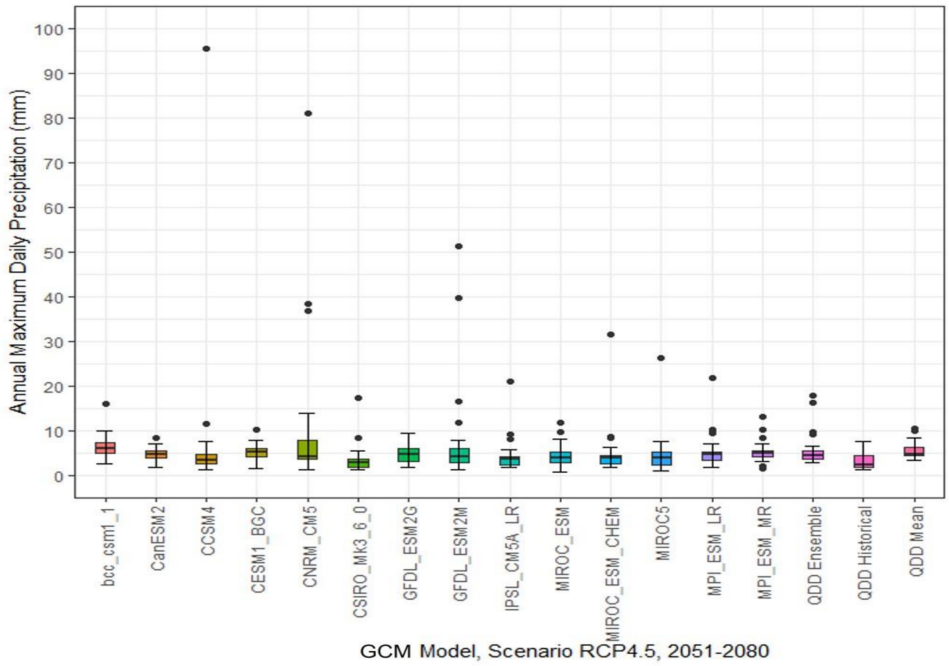

Figure 17. Boxplot for future projections of the annual maximum daily precipitation of 14 GCMs under the RCP4.5 scenario in the Devil's Creek, period 2051–2080. The linear extensions represent the highest and lowest values; the upper, middle and lower limits of the box represent the percentiles of 75%, 50%, and 25%, respectively; and the solid circles represent the outliers.

- RCP8.5 Scenario

The maximum annual precipitation projected for the period 2051–2080 under the RCP8.5 emission scenario in the Devil's Creek is shown in Figure 18. The results indicate a variation range from 0.62 mm to 224.65 mm with an average of 6.0 mm and a standard deviation of 10.50 mm for all models, indicating a high dispersion concerning the mean. The maximum value is projected by the bcc_csm1_1 (the Beijing Climate Center Climate System Model). Likewise, of the 14 models evaluated, 6 of them bcc_csm1_1, CanESM2, CNRM_CM5, GFDL_ESM2G, IPSL_CM5A_LR, MIROC5 projected the highest annual maximum precipitation values in a range from 19.28 mm to 224.65 mm, indicating that heavy rainfall could occur in the stream of the river. Diablo during the analysis period under this broadcast scenario.

On the other hand, the results of the model ensemble indicate a variation in the maximum annual precipitation from 2.92 mm to 49.74 mm, with an average of 7.21 mm for the 2051–2080 term under the RCP8.5 scenario. The range of uncertainty in the predictions is presented in Figure 19. Similarly, the linear extensions represent the highest and lowest values; the upper, middle, and lower limits of the box represent the percentiles of 75%, 50%, and 25%, respectively.

On the other hand, a relative change has been calculated in relation to the historical average for the period 1981–2005, simulated by the corrected and scaled GCM for the Devil's Creek. Under the RCP4.5 scenario, the annual maximum daily precipitation could increase by 32.44%, on average; with a range from −35.80% to +470.77%. Under the RCP8.5 scenario, the maximum annual precipitation will probably increase by 34.64%, on average, during the 2021–2050 term. Values range from −27.24% to 502.37%. Positive and negative values indicate a probable increase and decrease in the annual maximum daily precipitation, respectively. For the 2021–2050 period, under the RCP4.5 scenario, the maximum annual precipitation could increase by 29.79%, on average; the range is from −35.66% to +314.45%. On the other hand, under the RCP8.5 scenario, the maximum annual precipitation could increase by 67.23%, on average. For this scenario, the values range from

−32.24% to 1053.97%. The maximum percentage value corresponds to a positive anomaly of 45.43 mm concerning the historical average simulated by the GCM.

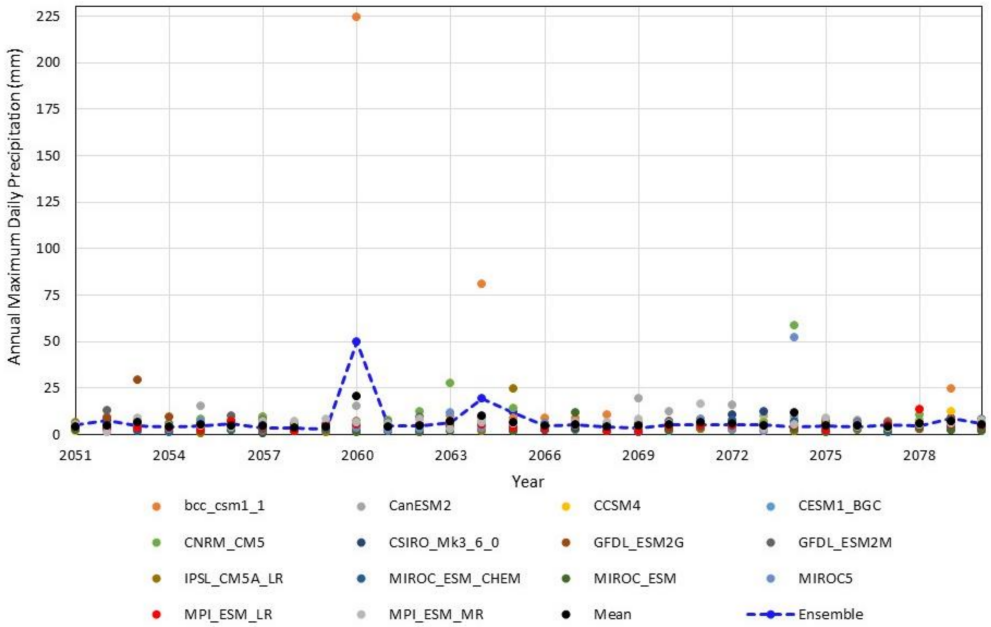

Figure 18. Annual maximum daily precipitation projected by 14 climate models under the RCP8.5 scenario for the Devil's Creek. The dashed blue line corresponds to the ensemble. Period: 2051–2080.

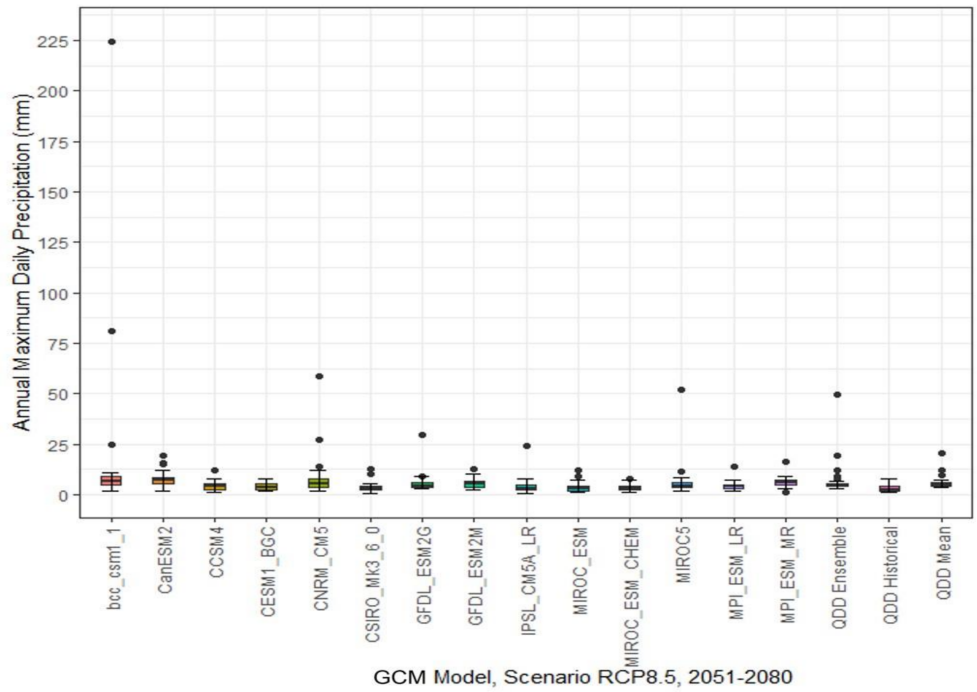

Figure 19. Boxplot for future projections of the annual maximum daily precipitation of 14 GCMs under the RCP8.5 scenario in the Devil's Creek, 2051–2080 term. The linear extensions represent the highest and lowest values; the upper, middle, and lower limits of the box represent the percentiles of 75%, 50%, and 25%, respectively; and the solid circles represent the outliers.

3.2. Projected Temperature

3.2.1. Annual Average Temperature

The temperature under climate change is another important variable that needs to be evaluated and projected to determine the potential impact on the hydrological response of the basin under study. Figures 20 and 21 present the minimum average annual temperature simulated by regional climate models, after bias correction and scaling for the study area, under RCP4.5 and RCP8.5 scenarios, for the 1981–2100 term. The black line corresponds to the averaged time series of all models evaluated. Similarly, as evidenced by other researchers, climate models agree in projecting a positive trend in temperature. However, from 2050 onwards, greater variability and a decrease in the trend are observed under the RCP4.5 scenario. On the other hand, as expected, the RCP8.5 high-emissions scenario projected the highest values. In both scenarios, the MIRO-ESM-CHEM model projects the highest minimum temperature values. Figures 22 and 23 show the average annual maximum temperature projected by the regional climate models for the study area, under the RCP4.5 and RCP8.5 scenarios, 1981–2100 term. Similarly, the black line corresponds to the averaged time series of all the evaluated models and for both scenarios, the MIRO-ESM-CHEM model projects the highest values of maximum temperature.

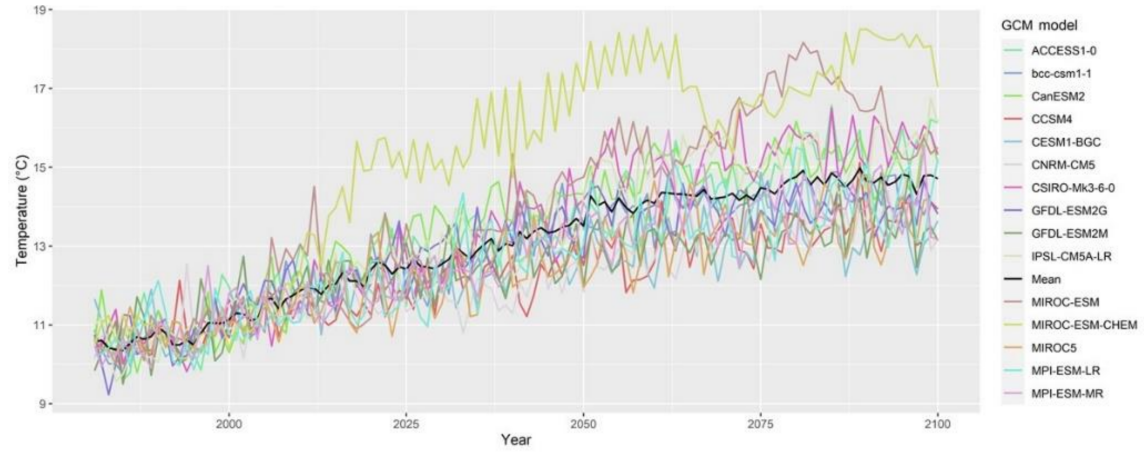

Figure 20. Minimum annual average temperature simulated by climate models, corrected and scaled for the Devil's Creek, 1981–2100 term, RCP4.5 emission scenario. The black line represents the averaged ensemble of 15 GCMs.

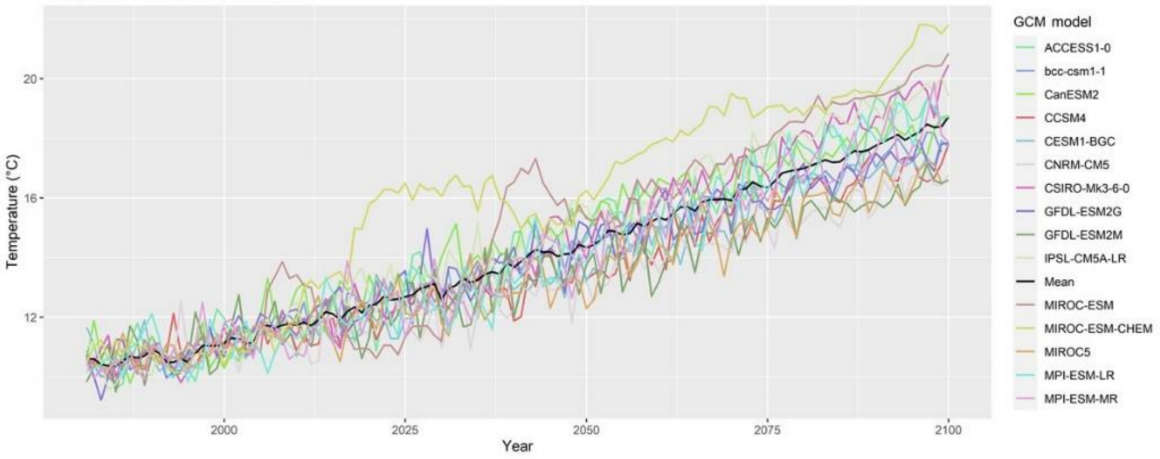

Figure 21. Minimum annual average temperature simulated by climate models, corrected and scaled for the Devil's Creek, 1981–2100 term, RCP8.5 emission scenario. The black line represents the averaged ensemble of the 15 GCMs.

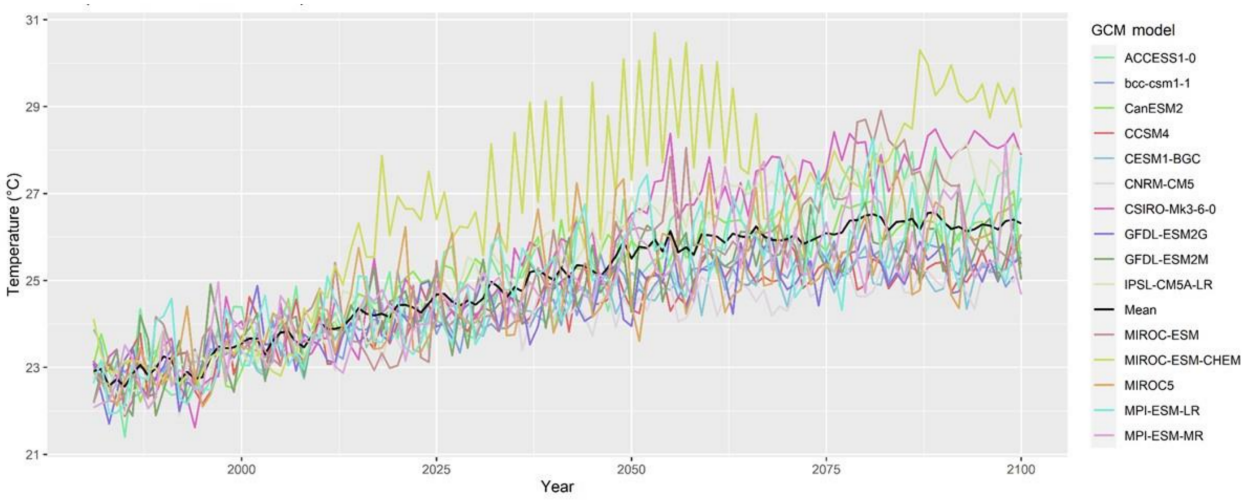

Figure 22. Maximum annual average temperature simulated by climate models, corrected and scaled for the Devil's Creek, 1981–2100 term, RCP4.5 emission scenario. The black line represents the averaged ensemble of 15 GCMs.

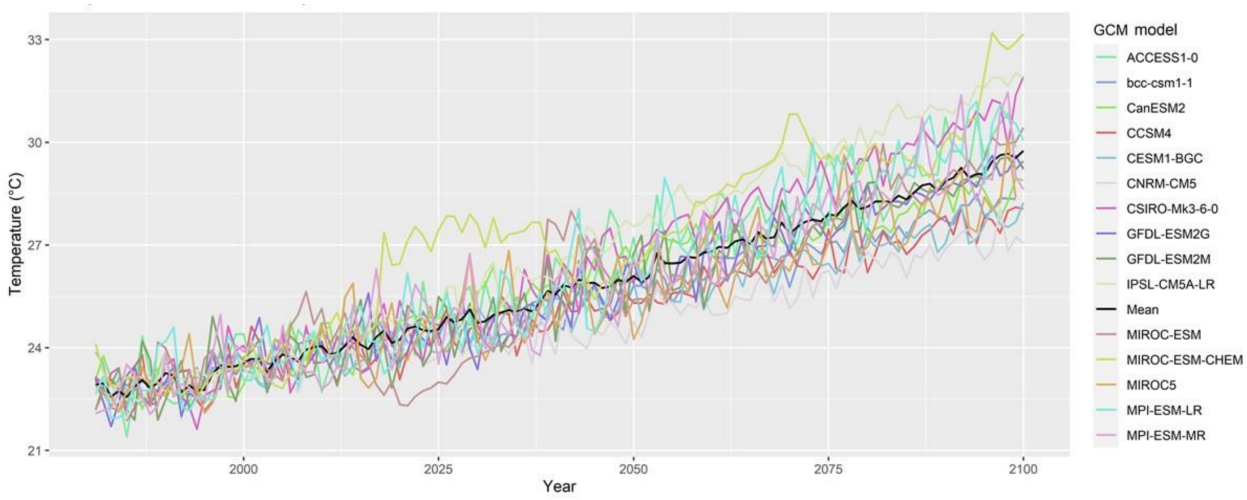

Figure 23. Maximum annual average temperature simulated by regional climate models, corrected and scaled for the Devil's Creek, 1981–2100 term, RCP8.5 emission scenario. The black line represents the averaged ensemble of 15 GCMs.

3.2.2. Average Monthly Temperature

Figure 24 presents the minimum monthly average temperature under the RCP4.5 and RCP8.5 scenarios for the Devil's Creek, 2021–2050 and 2051–2080 periods for the average multi-model ensemble of 15 regional climate models. Likewise, the historical period of 1981–2005 simulated by the GCM is observed. Monthly increases of 2.13 °C and 3.45 °C on average are projected for the minimum temperature under the RCP4.5 scenario, and of 2.62 °C and 4.90 °C under the RCP8.5 scenario, for the 2021–2050 and 2051–2080 terms, respectively. All of them corresponded with the 1981–2005 term. Likewise, the months of May, June, July, and August, as well as the period from January to March, project the largest increases in the minimum temperature for both scenarios. Figure 25 presents the maximum monthly average temperatures for the RCP4.5 and RCP8.5 scenarios. The results indicate an increase in the monthly average maximum temperature of 1.79 and 2.85 °C under the RCP4.5 scenario for the 2021–2050 and 2051–2080 terms, both relative to the 1985–2005 term. On the other hand, under the RCP8.5 scenario, the average increase is 2.12 °C and 4.06 °C for the periods previously described. For both scenarios, June, July, and August show the

largest increases, meaning that there will probably be greater warming during winter in the coming decades. Likewise, the minimum temperatures tend to increase slightly in relation to the maximum temperatures.

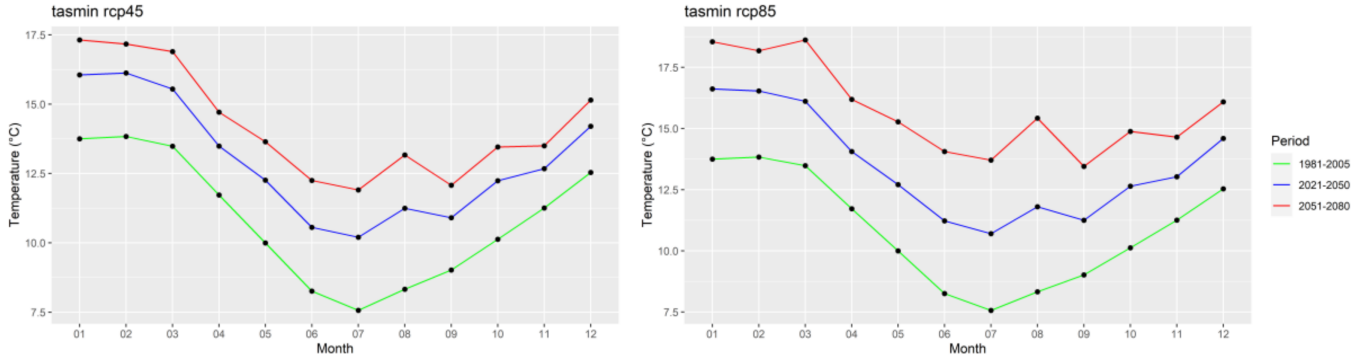

Figure 24. Average monthly temperature (minimum) under RCP4.5 and RCP8.5 scenarios for the Devil's Creek, 2021–2050 and 2051–2080 periods. The multi-model ensemble average of 15 GCMs.

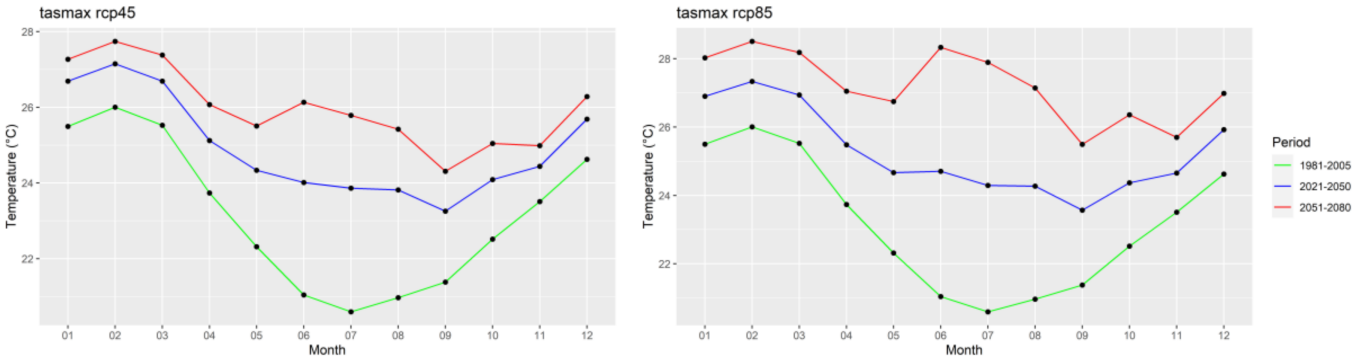

Figure 25. Average monthly temperature (maximum) under RCP4.5 and RCP8.5 scenarios for the Devil's Creek, 2021–2050 and 2051–2080 periods. The multi-model ensemble average of 15 GCMs.

3.2.3. Monthly Changes

In this study, we have provided average temperature changes for two periods: 2020–2050 and 2051–2080, relative to the period 1981–2005. Figure 26 shows the monthly average temperature changes (minimum) under RCP4.5 and RCP8.5 scenarios for the Devil's Creek, for the multi-model average ensemble of 15 GCMs corrected and downscaled. For both scenarios and the two study periods, changes are positives; consequently, minimum temperature would increase in the next decades under climate change. Under the RCP4.5 scenario, the largest positive changes are projected in July and August: 2.7 °C on average for the period 2021–2050. Additionally, this is a change of 4.4 °C, on average, for winter (JJA) during the period 2051–2080. The lowest minimum temperature changes are projected for spring (SON) with 1.8 °C and 2.9 °C for both periods, respectively. On the other hand, under the RCP8.5 scenario, the highest values of increase in the minimum temperature are projected for winter (JJA), more than 3.2 °C and 6. 3 °C for both periods.

Figure 27 shows the monthly average temperature change (maximum) under the RCP4.5 and RCP8.5 scenarios. Under the RCP4.5 scenario, it is evident that the greatest positive change in the maximum temperature would occur in winter (JJA), more than 3.0 °C and 4.9 °C for both periods. Similarly, for the RCP8.5 high-emissions scenario, in winter, the highest increases are projected, ranging from 3.5 to 6.9 °C, on average, for the periods 2021–2050 and 2051–2080, respectively.

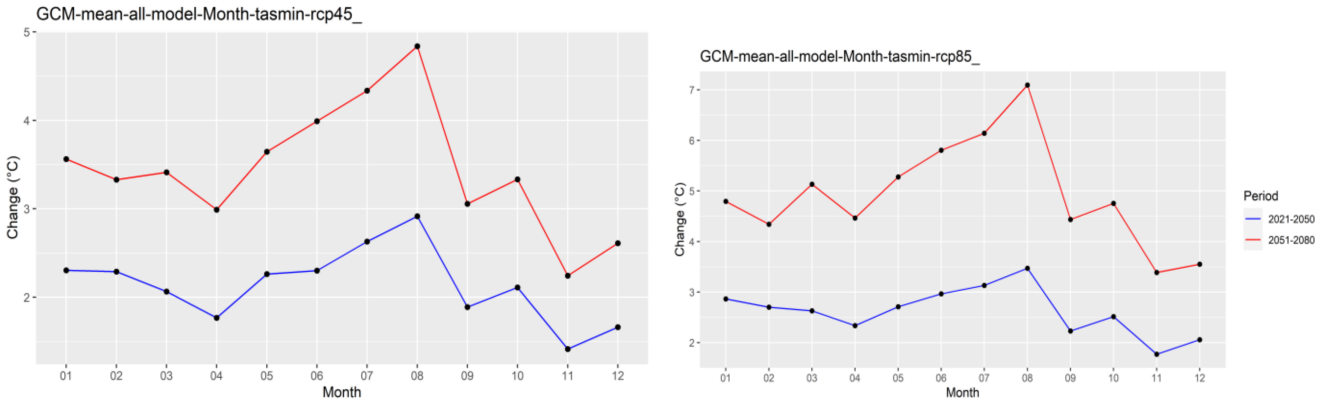

Figure 26. Average monthly temperature change (minimum) under RCP4.5 and RCP8.5 scenarios for the Devil's Creek, 2021–2050 and 2051–2080 periods. The multi-model ensemble average of 15 GCMs.

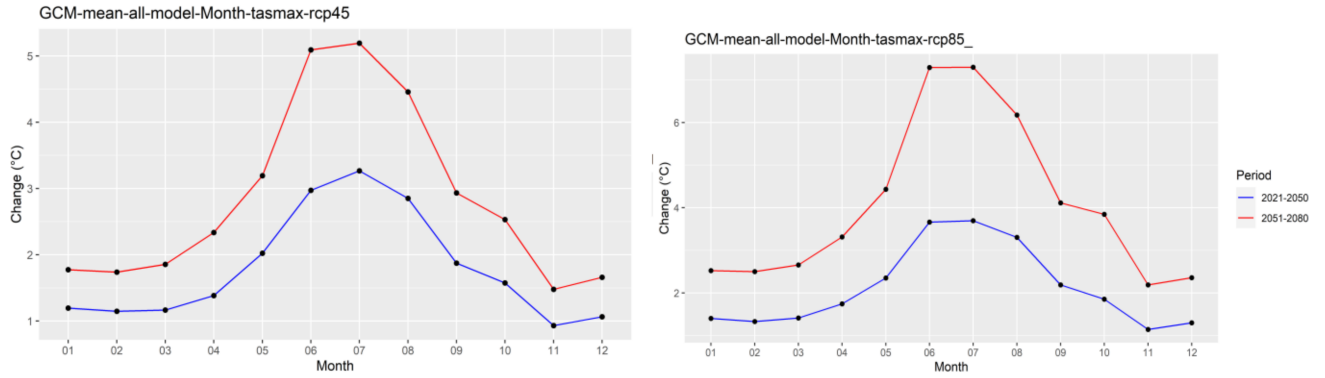

Figure 27. Average monthly temperature change (maximum) under RCP4.5 and RCP8.5 scenarios for the Devil's Creek, 2021–2050 and 2051–2080 periods. The multi-model ensemble average of 15 GCMs.

3.3. Calibration and Generation of Maximum Flows in the Devil's Creek

3.3.1. Under Historical Conditions

As a precedent to the generation of the maximum flows produced in the Devil's Creek, it should be mentioned that the channel of this creek was interrupted by an informal embankment used as a trail to access farms in the area of the Alto de la Alianza hill. The collapse of this embankment, located 2.0 km from the town of La Florida (City of Tacna), caused the debris flow on 21 February 2020. Figure 28 shows the site before and after the collapse of the informal embankment called Paso Camiara.

The calibration of the hydrological model was carried out by modeling the maximum flow produced in the Devil's Creek, dated 21 February 2020, as a result of the event of maximum rain and rupture of the Paso Camiara informal embankment. Figure 29 shows the topology of the Devil's Creek, generated in the RS Minerve model.

As seen in Figure 7, the Devil's Creek was subdivided into five sub-basins: two in the upper part (SC1 and SC2), two in the middle part (SC3 and SC4), and one in the lower part (SC5). Each of the sub-basins is linked to a virtual precipitation rain gauge. The precipitation events for each sub-basin are shown in Table 7.

The rain event of 21 February 2020, attributable to the positive anomaly of the sea surface temperature between +1 °C and +2 °C, produced off the coast of Tacna between 22 January 2020 and 22 February 2020 (Figure 30) [12].

Riverbed of the Devil's Creek obstructed by an informal embankment as an access trail to farms on the Alto de la Alianza hill. Source INGEMMET (2016).

The place of the informal embankment collapsed by the flood of 22 February 2020 and that caused the flood towards the city of Tacna.

Figure 28. Before and after the Devil's Creek channel was obstructed by an informal embankment as an access trail to farms in the Alto de la Alianza hill.

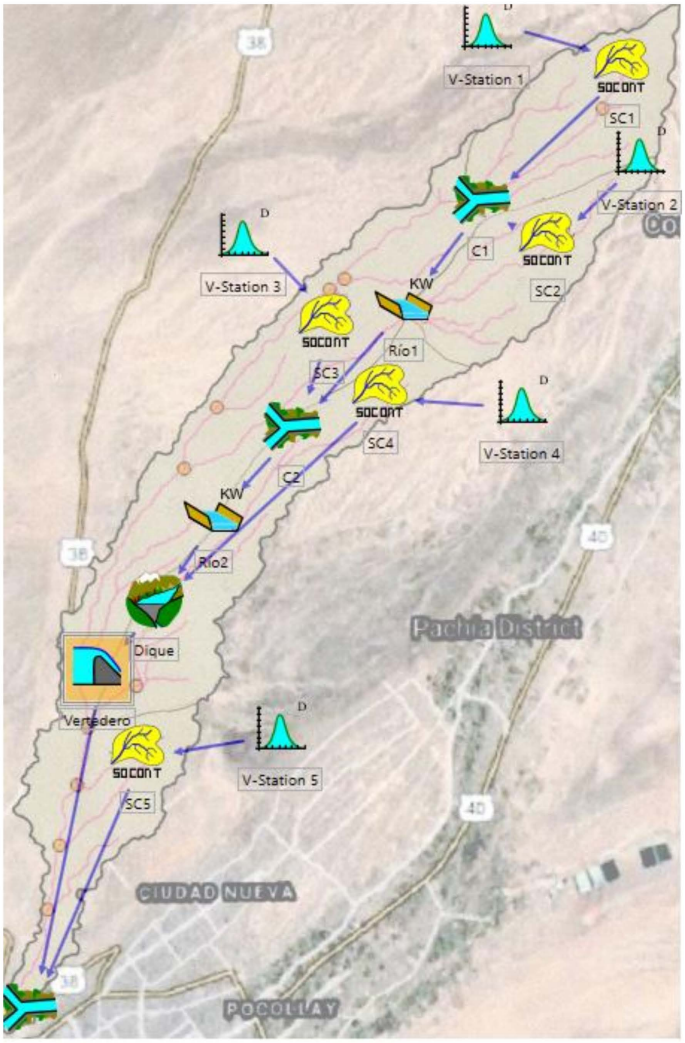

Figure 29. Structure of the RS Minerve Model for simulation of the 21 February 2020 event.

Table 7. The intensity of precipitation over each sub-basin (mm/h).

Date Hour	SC5	SC4 and SC3	SC2 and SC1
21 February 2020 15:00	0.00	0.00	0.00
21 February 2020 16:00	0.43	0.39	0.34
21 February 2020 17:00	2.03	1.83	1.62
21 February 2020 18:00	1.01	0.91	0.81
21 February 2020 19:00	5.36	4.82	4.29
21 February 2020 20:00	2.46	2.21	1.97
21 February 2020 21:00	0.86	0.77	0.69
21 February 2020 22:00	0.00	0.00	0.00

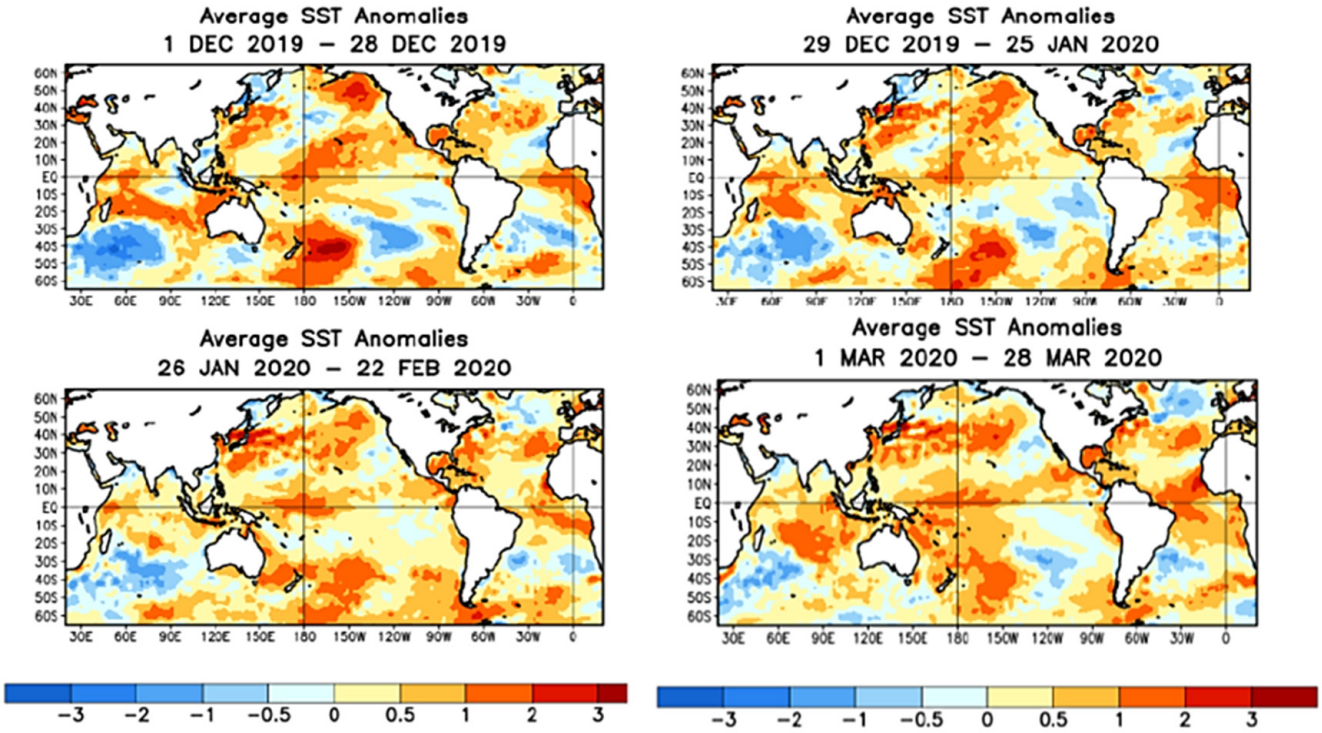

Figure 30. Sea surface temperature anomalies between 1 December 2019 and 28 March 2020.

Sub-basins 1 and 2 discharge their waters to River 1, and this flow joins the runoff produced by Sub-basin 3. This discharge feeds River 2, which joins the production of run-off from Sub-basin 4, before entering the informal Paso Camiara embankment. This structure served to model the dam break effect. Finally, the abrupt discharge from the dam break joins the runoff produced in Sub-basin 5. The parameters and initial conditions for each of the sub-basins are shown in Table 8. Likewise, the parameters and initial conditions for each river, are shown in Table 9.

In order to enter the RS Minerve, utilizing the bathymetry information of the Paso Camiara informal embankment (height vs. volume), the calculations were made using information from the topographic survey (Figure 31).

To simulate the dam break effect, it was assumed that this would occur when the dam's maximum height of 13.0 m was reached.

A necessary aspect to carry out the calculation of the dam break is the determination of the width of the breach.

To calculate the width of the rectangular breach (b), the formula proposed by Froehlich (2008) can be used, obtained by processing 69 cases of dam failures [46]:

$$b = 0.27\, k_0\, V^{0.32}\, H_b^{0.040} \quad (4)$$

where b (m) is the width of the breach, k_0 (Adim) is 1.3 (Overflow failures) and 1.0 (For other cases), V (m^3) is the volume of water stored above the bottom of the breach, and H_b (m) is the height of the breach.

Table 8. SOCONT model parameters for each sub-basin.

Sub-Basins		SC1	SC2	SC3	SC4	SC5
SOCONT Model Parameters						
A	m^2	8,446,871	7,775,105	16,991,236	8,542,694	11,086,674
bp	d/mm	0.0125	0.0125	0.0125	0.0125	0.0125
CFR	-	1	1	1	1	1
HGR3Max	m^2	0.1	0.1	0.1	0.2	0.5
J0	-	0.102	0.060	0.028	0.036	0.047
KGR3	1/s	0.001	0.001	0.001	0.001	0.001
Kr	$m^{1/3}/s$	2	2	2	2	2
L	m	1489.2	1301.7	1514.2	1008.1	1613.8
S	mm/°C/d	5	5	5	5	5
Sint	mm/°C/d	0	0	0	0	0
Smin	mm/°C/d	0	0	0	0	0
SPh	d	80	80	80	80	80
Tcf	°C	0	0	0	0	0
Tcp1	°C	0	0	0	0	0
Tcp2	°C	4	4	4	4	4
ThetaCri	-	0.1	0.1	0.1	0.1	0.1
Initial conditions						
SWEIni	m	0	0	0	0	0
ThetaIni	-	0	0	0	0	0
HGR3Ini	m	0.1	0.1	0.1	0.1	0.1
HrIni	m	0	0	0	0	0

Table 9. Riverbed model parameters by cinematic approximation.

Riverbed		River 1	River 2
Parameters			
L	m	12,541.4	8622.1
B0	m	5	12
m	-	1	1
J0	-	0.03	0.0335
K	$m^{1/3}/s$	30	30
N	-	1	1
Initial conditions			
Qini	m^3/s	0	0

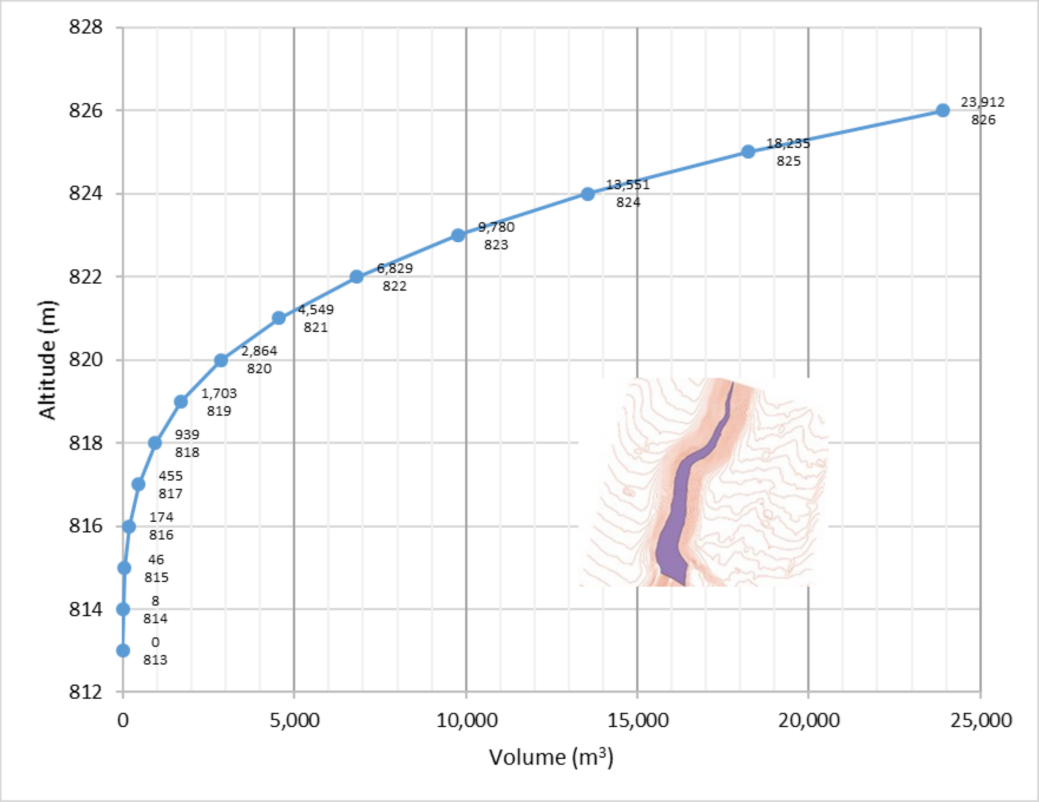

Figure 31. Bathymetry of the informal Paso Camiara embankment.

If we consider $k_0 = 1.3$, the volume of water stored before the dam break was 23,911.5 m^3, and if the total water height above the breach is 13.0 m, there will be a breach width of 9.8 m.

Likewise, if the breach is considered as a spillway, with a coefficient of 1.5, the discharge flow at the instant of the total rupture of the dam would be 688.7 m^3/s.

$$Q = 1.5 \times b \times Hmax^{1.5} = 1.5 \times 9.8 \times 13^{1.5} = 688.7\ m^3/s$$

The results of these calculations are shown in Table 10.

Table 10. Instantaneous discharge flow due to breach of the Paso Camiara informal embankment.

	Hc (m)	V (Hm^3)	b (m)	Qp (m^3/s)
Paso Camiara Dam	13	0.0239115	9.8	688.7

The simulated hydrographs produced by each of the sub-basins are shown in Figure 32.

The entrance hydrograph to the Paso Camiara informal embankment is shown in Figure 33. A maximum inflow flow of 10.72 m^3/s produced at 22:00 h was calculated. It should be mentioned that the Devil's Creek does not have a gauging station. The maximum flow of 10.72 m^3/s was contrasted with the water footprints left by the event in the riverbed of the Devil's Creek.

Figure 34 shows the height and flow hydrographs in the Paso Camiara dam. The results of the simulation show that from 4:00 p.m. on 21 February 2020, the filling of the Paso Camiara informal embankment began, breaking at a maximum water height of 15.7 m and discharging a maximum flow of 2550.8 m^3/s. Figure 35 shows the debris flow which produced floods that caused the loss of three human lives as well as great economic losses in Tacna city.

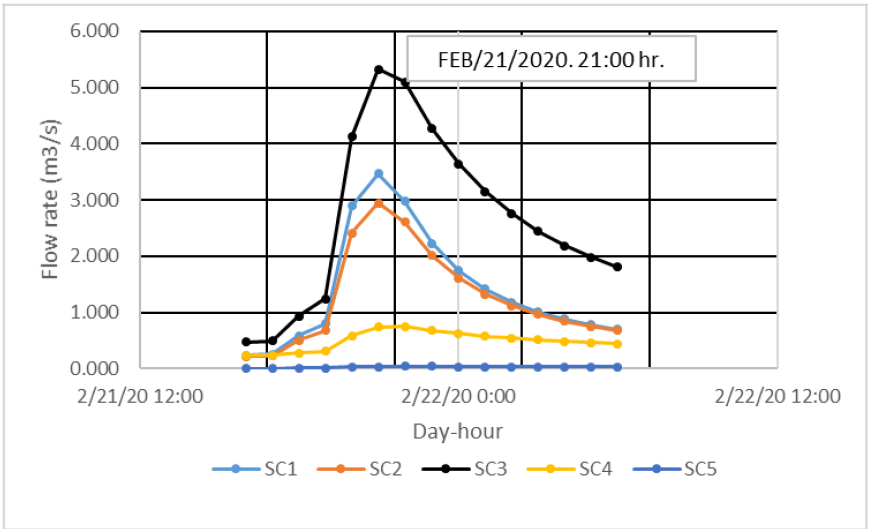

Figure 32. Hydrographs generated by the sub-basins.

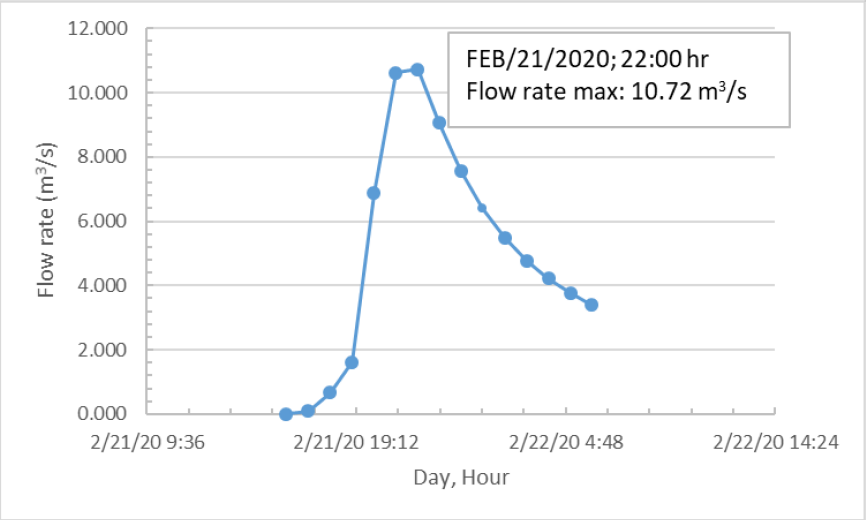

Figure 33. Hydrograph of entry to the Paso Camiara informal embankment.

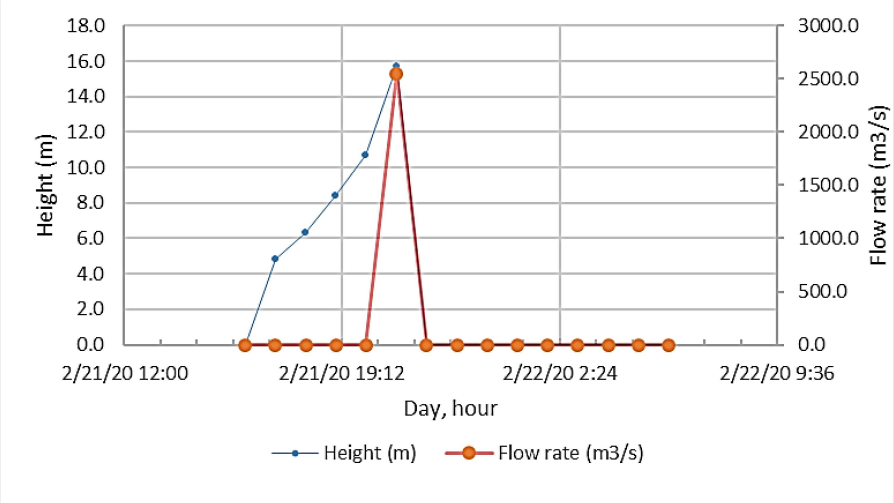

Figure 34. Hydrographs of water height in the dam and flow discharged due to the collapse of the Paso Camiara dam.

Figure 35. Gestion newspaper reports: debris flow in Tacna left three people dead, 22 February 2020.

3.3.2. Under Climate Change Conditions

To carry out the hydrological modeling of the maximum flow in the Devil's Creek, produced by maximum rainfall events generated by climate change models, a topology was used without considering the Paso Camiara informal embankment. Therefore, Sub-basins 1 and 2 discharge their waters to River 1, and this flow joins the runoff produced by Sub-basin 3. This discharge feeds River 2, which joins the production of run-off from Sub-basin 4, which joins the runoff produced in Sub-basin 5. Likewise, the parameters and initial conditions for each of the sub-basins were maintained. Figure 36 shows the structure of the RS Minerve model.

The modeling of the maximum flow product of precipitation intensities over each sub-basin (mm/h) for the RCP4.5 and 8.5 scenarios, and for 2021–2050 and 2051–2080 terms (Table 11), are shown in Table 12 and Figure 37, respectively.

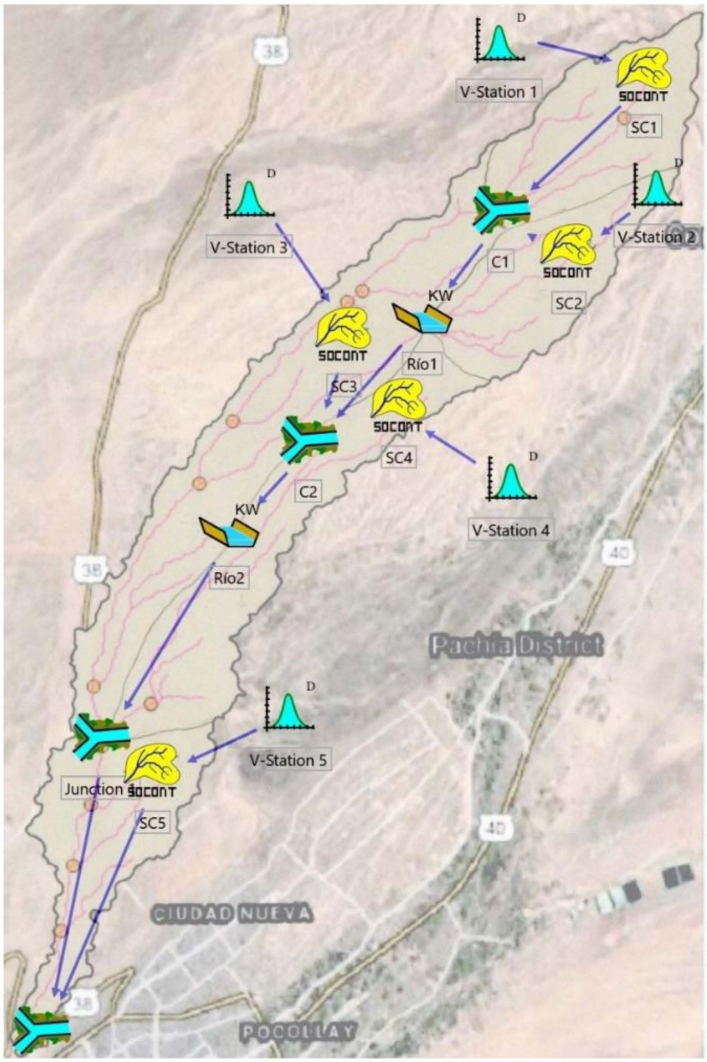

Figure 36. Structure of the RS Minerve Model for the simulations of events with different climate change scenarios.

Table 11. Precipitation intensity over each sub-basin (mm/h) for RCP4.5 and 8.5 scenarios, from 2021 to 2050 and from 2051 to 2080.

	2021–2050 (RCP4.5)			2051–2080 (RCP4.5)			2021–2050 (RCP8.5)			2051–2080 (RCP8.5)		
Hours	**SC5**	**SC4 and SC3**	**SC2 and SC1**	**SC5**	**SC4 and SC3**	**SC2 and SC1**	**SC5**	**SC4 and SC3**	**SC2 and SC1**	**SC5**	**SC4 and SC3**	**SC2 and SC1**
0	0.00	0.00	0.00	0.00	0.00	0.00	0.00	0.00	0.00	0.00	0.00	0.00
1	0.87	0.78	0.70	0.63	0.57	0.51	0.92	0.83	0.73	1.76	1.58	1.41
2	4.11	3.70	3.29	2.98	2.69	2.39	4.34	3.90	3.47	8.31	7.48	6.65
3	2.04	1.84	1.64	1.48	1.34	1.19	2.16	1.94	1.73	4.13	3.72	3.31
4	10.85	9.77	8.68	7.88	7.09	6.30	11.45	10.31	9.16	21.94	19.75	17.55
5	4.98	4.48	3.98	3.62	3.25	2.89	5.26	4.73	4.20	10.07	9.06	8.06
6	1.74	1.57	1.39	1.26	1.14	1.01	1.84	1.65	1.47	3.52	3.17	2.82
7	0.00	0.00	0.00	0.00	0.00	0.00	0.00	0.00	0.00	0.00	0.00	0.00
Total in 6 h	24.60	22.14	19.68	17.86	16.07	14.29	25.96	23.36	20.77	49.74	44.77	39.79

Table 12. Flood hydrographs for RCP4.5 and RCP8.5 scenarios from 2021 to 2050 and from 2051 to 2080.

Time (Hour)	Years 2021–2050 RCP4.5	Years 2021–2050 RCP8.5	Years 2051–2080 RCP4.5	Years 2051–2080 RCP8.5
1.0	0.0	0.0	0.0	0.0
2.0	0.1	0.1	0.1	0.2
3.0	2.2	2.5	1.2	14.0
4.0	4.9	5.5	2.9	16.6
5.0	23.7	26.0	13.5	76.4
6.0	30.4	32.9	19.1	78.6
7.0	26.0	27.7	17.6	55.7
8.0	19.1	20.1	13.8	34.9
9.0	14.4	15.1	10.9	23.9
10.0	11.3	11.7	8.9	17.5
11.0	9.1	9.5	7.4	13.4
12.0	7.6	7.8	6.3	10.7
13.0	6.4	6.6	5.4	8.7
14.0	5.5	5.7	4.7	7.3
15.0	4.9	5.0	4.2	6.3

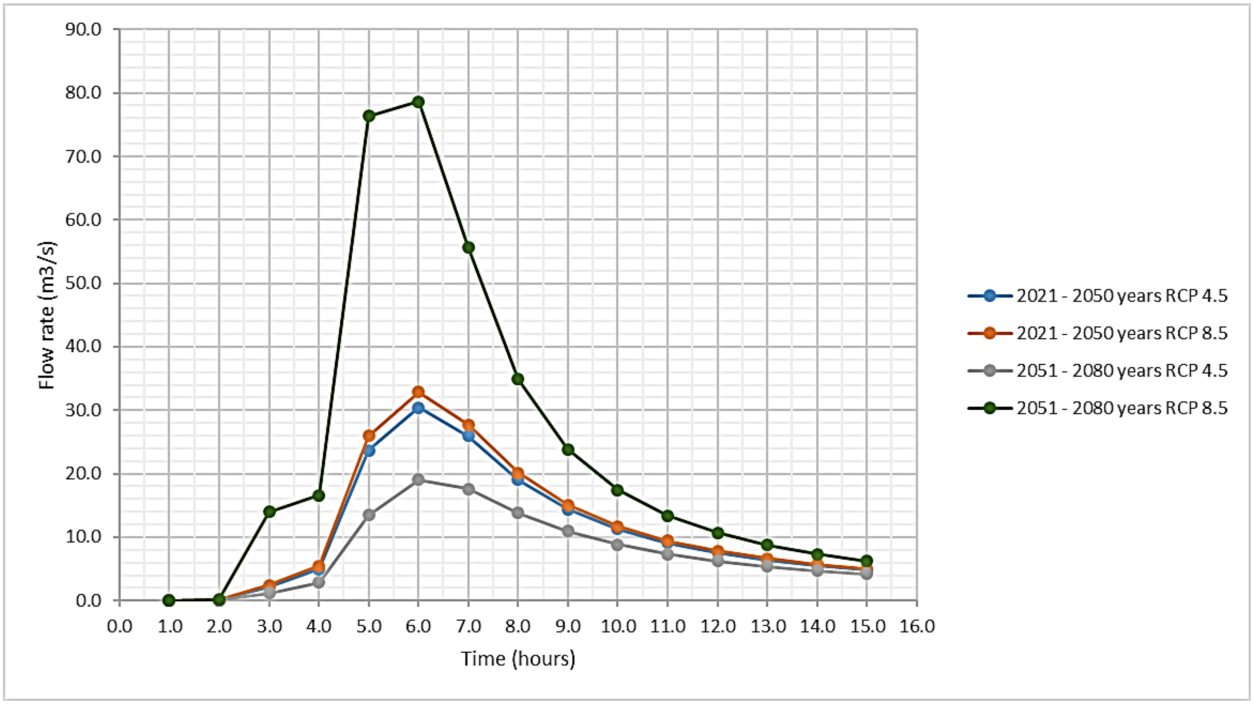

Figure 37. Flood hydrographs for RCP4.5 and RCP8.5 scenarios for 2021–2050 and 2051–2080 terms.

4. Discussion

This research addressed the impacts of natural variability and climate change on the maximum precipitation and maximum flows in the Devil's Creek, Tacna, Peru. For the projection of the future maximum annual precipitation, maximum temperature, and minimum temperature, the analysis is based on the daily output of 15 general circulation models (GCMs) of the CMIP5 project (Coupled Model Intercomparison Project Phase 5) and

considers two emission scenarios: RCP4.5 and RCP8.5. The Access1-0 model projection was discarded due to a high overestimation of maximum precipitation. Furthermore, given the uncertainty in the projections by the GCMs [31], an ensemble of 14 GCMs was assessed. In general, although most models do not agree in projecting similar trends in precipitation as evidenced in other investigations [21,45,46], the projections indicate that the future pattern of maximum annual precipitation will experience significant changes, with increases for the two periods evaluated and for both scenarios.

Compared with historical conditions, heavy precipitation events are intensified, especially for the high-emissions scenario, according to the multi-model ensemble of 14 GCMs. Under the RCP4.5 scenario, the maximum annual precipitation could increase by more than 32%, on average, whereas under the RCP8.5 scenario, it could increase by 35%, on average, during the 2021–2050 period relative to the historical period of 1981–2005. On the other hand, for the 2051–2080 period, the maximum annual precipitation projected for the RCP4.5 scenario tends to decrease slightly. However, significant positive change is projected under the RCP8.5 scenario relative to the 1981–2005 period.

Regarding future temperature changes, as evidenced in other investigations, the GCMs agree in projecting a positive temperature trend [47,48]. However, as of 2050, greater variability and a decrease in the low trend are observed under the RCP4.5 scenario for the Devil's Creek area. Additionally, as expected, the RCP8.5 scenario projected the highest temperature values. For both scenarios, the values in June, July, and August denote a high range of positive changes of the minimum temperature. The behavior is similar for the monthly average maximum temperature during the 2021–2050 term for both scenarios. In contrast, it occurs during the 2050–2080 term under the RCP8.5 scenario that indicates significant warming during June, July, and August; similarly, it happens for January, February, and March.

Regarding the historical rainfall event of 21 February 2020, in the Devil's Creek, it can be affirmed that this is attributable to the positive anomaly of the sea surface temperature off the coast of Tacna during the days before that date.

Likewise, the lowest estimated rainfall sheet for the event of 21 February 2020, in the Devil's Creek, concerning the rainfall sheet recorded in the city of Tacna, is attributed to the shorter distance from the city of Tacna to the coastal area. This was demonstrated, in the absence of registered information on rainfall on the Devil's Creek, through the spatio-temporal analysis of the information registered in the city of Tacna (JORGE BASADRE rain gauge) and satellite products such as IMERG and CHIRPS.

Regarding the debris flow produced as a result of the rainfall event of 21 February 2020, which caused a loss of human lives, this was the consequence of the collapse of an informal embankment built as a trail, located 2.0 km upstream from the town center named La Florida (City of Tacna).

Regarding the historical and future hydrological modeling, these were carried out through the RS Minerve program. The historical hydrological modeling was calibrated by estimating the footprints of maximum flows produced in the middle section of the Devil's Creek and the evidence and testimonies recorded in videos of the magnitude of the disaster caused by the debris flow of 21 February 2020. The future hydrological modeling was carried out for two time periods: 2021 to 2050 and 2051 to 2080, for RCP4.5 and RCP8.5 scenarios, respectively. The results will be used for the design of studies and alternatives for the protection of the population in the area of influence of the Devil's Creek.

5. Conclusions

Climate models agree in projecting a positive trend in surface temperature. However, from 2050 onwards, greater variability and a decrease in the trend were observed under the RCP4.5 scenario. On the other hand, as expected, the RCP8.5 high-emissions scenario projected the highest values. For both scenarios and for both periods, minimum and maximum temperature would increase under climate change. Higher positive monthly changes are projected in June, July, and August, meaning that winters would be warmer.

The result of the model ensemble, under the RCP4.5 scenario, indicated a variation in the maximum annual precipitation from 2.77 mm to 24.70 mm, with an average of 5.70 mm for the 2021–2050 term. Additionally, this was from 3.14 mm to 25.96 mm, with an average of 5.80 mm under the RCP8.5 scenario. For the 2051–2080 term, the multi-model ensemble of 14 GCMs indicated a variation in the maximum annual precipitation from 2.77 mm to 17.86 mm, with an average of 5.60 mm under the RCP4.5 scenario and from 2.92 mm to 49.74 mm, averaging 7.21 mm under the RCP8.5 scenario.

Regarding the relative change, under the RCP4.5 scenario, the maximum annual precipitation could increase by 32%, on average. Under the RCP8.5 scenario, it would probably increase by 35%, on average, during the 2021–2050 term. On the other hand, for the 2050–2080 term, the maximum annual precipitation could increase by 30% under the RCP4.5 scenario and 65% under the RCP8.5 scenario.

The rainfall event of 21 February 2020, in the Devil's Creek, is attributable to the positive anomaly of the sea surface temperature between +1 °C and +2 °C, produced off the coast of Tacna between 22 January 2020, and 22 February 2020.

The debris flow produced as a result of the rainfall event of 21 February 2020 was the consequence of the collapse of an informal embankment built as a trail, located 2.0 km upstream from the town of La Florida (City of Tacna).

Historical hydrological modeling using the RS Minerve model was calibrated by estimating the footprints of maximum flows produced in the middle section of the Devil's Creek and the evidence and testimonies recorded in videos of the magnitude of the disaster caused by the debris flow of 21 February 2020.

The maximum flood volume in the Devil's Creek could increase by 220% and 154% for the RCP4.5 scenario, for the 2021–2050 and 2051–2080 terms, respectively.

The maximum flood volume in the Devil's Creek could increase by 234% and 484% for the RCP8.5 scenario for the 2021–2050 and 2051–2080 terms, respectively.

Author Contributions: E.I.-B. designed, collected observed data, wrote the first draft, and edited the document. E.C.-V. designed, collected observed data, wrote the first draft, and edited the document. E.P.-V. guided writing and review. F.M., A.C. and A.V. collected and processed information. All authors have read and agreed to the published version of the manuscript.

Funding: Universidad Nacional Jorge Basadre Grohmann, Tacna, Perú.

Institutional Review Board Statement: Not applicable.

Informed Consent Statement: Not applicable.

Data Availability Statement: Not applicable. The data corresponds to reports from Peruvian public institution that under agreement provided such information with academic purposes.

Acknowledgments: The authors would like to thank the National Water Authority (ANA) and the National Meteorology and Hydrology Service (SENAMHI) for providing the valuable information used in this work.

Conflicts of Interest: The authors declare no conflict of interest.

References

1. Ingol, E.M.; Mckinney, D.C. *Modeling Climate Change Impacts on Hydrology and Water Resources: Case Study Rio Conchos Basin*; Center for Research in Water Resources Bureau of Engineering Research, The University of Texas at Austin: Austin, TX, USA, 2011.
2. Stagl, J.; Mayr, E.; Koch, H.; Hattermann, F.; Huang, S.; Judith, S. *Managing Protected Areas in Central and Eastern Europe Under Climate Change, Effects of Climate Change on the Hydrological Cycle in Central and Eastern Europe*; Springer Open: Berlin/Heidelberg, Germany, 2013; pp. 31–43.
3. IPCC. *Climate Change and Water. Contribution to the Fourth Assessment Report of the Intergovernmental Panel on Climate Change*; Bates, B.C., Kundzewicz, Z.W., Wu, S., Palutikof, J.P., Eds.; IPCC Technical Paper VI; IPCC: Geneva, Switzerland, 2008.
4. SENAMHI. Escenarios Climáticos en el Perú para el Año 2030. 2009. Available online: https://idesep.senamhi.gob.pe/portalidesep/files/tematica/cambio_climatico/Escenarios_climaticos_en_el_Peru_para_el_ano_2030.pdf (accessed on 21 November 2021).

5. Changnon, S.A. *El Niño 1997–1998: The Climate Event of the Century*; Oxford University Press: New York, NY, USA, 2000; p. 36. ISBN 978-0-19-803096-6. Available online: https://oxford.universitypressscholarship.com/view/10.1093/oso/9780195135510.001.0001/isbn-9780195135510 (accessed on 21 November 2021).
6. Comunidad Andina de Fomento (CAF). El Fenomeno El Niño 1997–1998 Memoria; Retos Y Soluciones. 2000. Available online: https://scioteca.caf.com/bitstream/handle/123456789/676/Las%20lecciones%20de%20El%20Ni%C3%B1o.Per%C3%BA.pdf (accessed on 21 November 2021).
7. El Niño Costero. *Las Inundaciones de 2017 en el Perú*; ISET-International, Soluciones Prácticas y el Programa de Resiliencia a las Inundaciones de Zúrich: La Paz, Bolivia, 2017.
8. Pino, E.; Ramos, L.; Avalos, O.; Tacora, P.; Chávarri, E.; Angulo, O.; Ascensios, D.; Mejía, J. Effect of Environmental and Geological Characteristics on Water Quality in the Caplina River Basin, Tacna, Peru. *Tecnol. Cienc. Agua* **2017**, *8*, 77–99. [CrossRef]
9. Cheng, L.; AghaKouchak, A. Nonstationary Precipitation Intensity-Duration-Frequency Curves for Infrastructure Design in a Changing Climate. *Sci. Rep.* **2014**, *4*, 7093. [CrossRef]
10. Sarhadi, A.; Soulis, E.D. Time-varying extreme rainfall intensity-duration-frequency curves in a changing climate. *Geophys. Res. Lett.* **2017**, *44*, 2454–2463. [CrossRef]
11. Hu, H.; Ayyub, B. Extreme Precipitation Analysis and Prediction for a Changing Climate. *ASCE-ASME J. Risk Uncertain. Eng. Syst. Part A Civ. Eng.* **2018**, *4*, 04018029. [CrossRef]
12. Pino, E.; Chávarri, E. Evidence of climate change in the hyper-arid region of the southern coast of Peru, head of the Atacama Desert. *Tecnol. Cienc. Agua* **2022**, *3*, 1. [CrossRef]
13. CMIP5. Coupled Model Intercomparison Project Phase 5. 2013. Available online: https://pcmdi.llnl.gov/mips/cmip5/ (accessed on 21 November 2021).
14. Han, Z.Y.; Tong, Y.; Gao, X.J. Correction based on quantile mapping for temperature simulated by the RegCM4. *Clim. Change Res.* **2018**, *14*, 331–340.
15. Yang, X.; Wood, E.F.; Sheffield, J.; Ren, L.; Zhang, M.; Wang, Y. Bias correction of historical and future simulations of precipitation and temperature for china from CMIP5 models. *J. Hydrometeorol.* **2018**, *19*, 609–623. [CrossRef]
16. Tong, Y.; Gao, X.; Han, Z.; Xu, Y.; Xu, Y.; Giorgi, F. Bias correction of temperature and precipitation over China for RCM simulations using the QM and QDM methods. *Clim. Dyn.* **2021**, *57*, 1425–1443. [CrossRef]
17. Paulhus, J.L.H.; Kohler, M.A. Interpolation of missing precipitation records. *Mon. Weather. Rev.* **1952**, *80*, 129–133. [CrossRef]
18. Guijarro, J.A. Homogenization of climatic series with Climatol. In *Reporte Técnico State Meteorological Agency (AEMET)*; Balearic Islands Office: Madrid, Spain, 2018.
19. Aybar, C.; Lavado-Casimiro, W.; Huerta, A.; Fernández, C.; Vega, F.; Sabino, E.; Felipe-Obando, O. Uso del Producto Grillado "PISCO" de Precipitación en Estudios, Investigaciones y Sisitemas Operacionales de Monitoreo y Pronóstico Hidrometeorológico. 2017. Available online: https://www.senamhi.gob.pe/load/file/01402SENA-8.pdf (accessed on 21 November 2021).
20. Warren, W.; Parkinson, C. *An Introduction to Three-Dimensional Climate Modeling*, 2nd ed.; University Science Books; National Center for Atmospheric Research and NASA Goddard Space Flight Center: California, VA, USA, 2005; p. 368.
21. IPCC. *Climate Change 2013: The Physical Science Basis. Contribution of Working Group I to the Fifth Assessment Report of the Intergovernmental Panel on Climate Change*; Stocker, T.F.D., Qin, G.-K., Plattner, M., Tignor, S.K., Allen, J., Boschung, A., Nauels, Y., Xia, V.B., Midgley, P.M., Eds.; Cambridge University Press: Cambridge, UK, 2013; p. 1535.
22. Flato, G.J.; Marotzke, B.; Abiodun, P.; Braconnot, S.C.; Chou, W.; Collins, P.; Cox, F.; Driouech, S.; Emori, V.; Eyring, C.; et al. Evaluation of climate models. In *Climate Change 2013: The Physical Science Basis. Contribution of Working Group I to the Fifth Assessment Report of the Intergovernmental Panel on Climate Change*; Cambridge University Press: Cambridge, UK.
23. Overland, J.E.; Wang, M.; Bond, N.A.; Walsh, J.E.; Kattsov, V.M.; Chapman, W.L. Considerations in the Selection of Global Climate Models for Regional Climate Projections: The Arctic as a Case Study. *J. Clim.* **2011**, *24*, 1583–1597. [CrossRef]
24. NASA. NEX-GDDP: NASA Earth Exchange Global Daily Downscaled Climate Projections, the Coupled Model Intercomparison Project Phase 5. 2012. Available online: https://www.nccs.nasa.gov/sites/default/files/NEX-GDDP-CMIP6-Tech_Note.pdf (accessed on 21 November 2021).
25. Wilby, R.L.; Wigley, T.M.L. Downscaling General Circulation Model Ouput: Review of Methods and Limitations. *Prog. Phys. Geogr.* **1997**, *21*, 530–548. [CrossRef]
26. Chong-Yu, X. From GCMs to River Flow: A Review of Downscaling Methods and Hydrologic Modeling Approach. *Prog. Phys. Geogr.* **1999**, *23*, 229–249.
27. Wilby, R.L.; Charles, S.P.; Zorita, E.; Timbal, B.; Whetton, P.; Mearns, L.O. Guidelines for Use of Climate Scenarios Developed From Statistical Downscaling Methods. 2004. Available online: https://www.ipcc-data.org/guidelines/dgm_no2_v1_09_2004.pdf (accessed on 21 November 2021).
28. Fowler, H.J.; Blenkinsop, S.; Tebaldi, C. Linking climate change modeling to impacts studies: Recent advances in downscaling techniques for hydrological modeling. *Int. J. Clim.* **2007**, *27*, 1547–1578. [CrossRef]
29. Teutschbein, C.; Seiber, J. Bias correction of regional climate model simulations for hydrological climate-change impact studies: Review and evaluation of different methods. *J. Hydrol.* **2012**, *456–457*, 12–29. [CrossRef]
30. Maraun, G. Bias Correction, Quantile Mapping, and Downscaling: Revisiting the Inflation Issue, Helmholtz Centre for Ocean Research Kiel, Kiel, Germany. *J. Clim.* **2013**, *26*, 2137–2143. [CrossRef]

31. Perkins, S.E.; Fischer, E.M. The usefulness of different realizations for the model evaluation of regional trends in heat waves. *Geophys. Res. Lett.* **2013**, *40*, 5793–5797. [CrossRef]
32. Semenov, M.; Stratonovitch, P. Use of multi-model ensembles from global climate models for assessment of climate change impacts. *Clim. Res.* **2010**, *41*, 1–14. [CrossRef]
33. Bishop, C.H.; Abramowitz, G. Climate model dependence and the replicate Earth paradigm. *Clim. Dyn.* **2013**, *41*, 885–900. [CrossRef]
34. LeDuc, M.; Mailhot, A.; Frigon, A.; Martel, J.-L.; Ludwig, R.; Brietzke, G.B.; Giguère, M.; Brissette, F.; Turcotte, R.; Braun, M.; et al. The ClimEx Project: A 50-Member Ensemble of Climate Change Projections at 12-km Resolution over Europe and Northeastern North America with the Canadian Regional Climate Model (CRCM5). *J. Appl. Meteorol. Clim.* **2019**, *58*, 663–693. [CrossRef]
35. Annan, J.D.; Hargreaves, J.C. On the meaning of independence in climate science. *Earth Syst. Dyn.* **2017**, *8*, 211–224. [CrossRef]
36. Wang, B.; Zheng, L.; Liu, D.L.; Ji, F.; Clark, A.; Yu, Q. Using multi-model ensembles of CMIP5 global climate models to reproduce observed monthly rainfall and temperature with machine learning methods in Australia. *Int. J. Clim.* **2018**, *38*, 4891–4902. [CrossRef]
37. Holland, J.H. Genetic algorithms. *Sci. Am.* **1992**, *267*, 44–50. [CrossRef]
38. Kramer, O. Genetic algorithms. In *Genetic Algorithm Essentials*; Springer: Berlin/Heidelberg, Germany, 2017; pp. 11–19.
39. SENAMHI. Boletín Hidroclimático Mensual Dirección Zonal 7. 2021. Available online: https://repositorio.senamhi.gob.pe/handle/20.500.12542/1209 (accessed on 21 November 2021).
40. Krause, P.; Boyle, D.P.; Bäse, F. Comparison of different efficiency criteria for hydrological model assessment. *Adv. Geosci.* **2005**, *5*, 89–97. [CrossRef]
41. Moriasi, D.N.; Gitau, M.W.; Pai, N.; Daggupati, P. Hydrologic and Water Quality Models: Performance Measures and Evaluation Criteria. *Trans. ASABE* **2015**, *58*, 1763–1785. [CrossRef]
42. Muñoz, R.; Huggel, C.; Drenkhan, F.; Vis, M.; Viviroli, D. Comparing model complexity for glacio-hydrological simulation in the data-scarce Peruvian Andes. *J. Hydrol. Reg. Stud.* **2021**, *37*, 100932. [CrossRef]
43. Hidalgo, I.G.; Paredes-Arquiola, J.; Andreu, J.; Lerma-Elvira, N.; Lopes, J.E.G.; Cioffi, F. Hydropower generation in future climate scenarios. *Energy Sustain. Dev.* **2020**, *59*, 180–188. [CrossRef]
44. Astorayme, M.; García, J.; Suarez, W.; Felipe, O.; Huggel, C.; Molina, W. Modelización hidrológica con un enfoque semidistribuido en la cuenca del río Chillón, Perú. *Rev. Peru. Geo Atmosférica RGPA* **2015**, *4*, 109–124. Available online: http://www.senamhi.gob.pe/rpga/pdf/2015_vol04/paper8.pdf (accessed on 21 November 2021).
45. Garcia, J.; Foehn, A.; Fluixa, J.; Roquire, B.; Brauchli, T.; Paredes, J.; Cesare, G.; Minerve, R.S. *Technical Manual*; Centre de Recherche sur l'Environnement Alpin: Sion, Switzerland, 2020.
46. Campos, D. Modelado empírico simple del rompimiento de presas pequeñas de tierra (hidrograma de salida). *Ing. Investig. Tecnol.* **2013**, *14*, 377–388. [CrossRef]
47. Dosio, A.; Jones, R.G.; Jack, C.; Lennard, C.; Nikulin, G.; Hewitson, B. What can we know about future precipitation in Africa? Robustness, significance and added value of projections from a large ensemble of regional climate models. *Clim. Dyn.* **2019**, *53*, 5833–5858. [CrossRef]
48. Ortega, G.; Arias, P.A.; Villegas, J.C.; Marquet, P.A.; Nobre, P. Present-day and future climate over central and South America according to CMIP5/CMIP6 models. *Int. J. Clim.* **2021**, *41*, 6713–6735. [CrossRef]